



RESEARCH ARTICLE

10.1029/2018JB015941

Key Points:

- Nature and evolution of mudstone pore systems are quantified as a function of: texture, mineralogy, organic matter content, and thermal maturity
- Pore systems are well connected across the full nanometer-micrometer spectrum of pore sizes; connected networks occur mainly through pores with <10-nm radius
- Multiphase flow is influenced not only by connectivity of pores but also larger-scale connectivity of clay-rich and organocarbonate domains

Correspondence to:

E.J. Mathia,
elizamathia@chemostrat.com

Citation:

Mathia, E. J., Rexer, T. F. T., Thomas, K. M., Bowen, L., & Aplin, A. C. (2019). Influence of clay, calcareous microfossils, and organic matter on the nature and diagenetic evolution of pore systems in mudstones. *Journal of Geophysical Research: Solid Earth*, 124, 149–174. <https://doi.org/10.1029/2018JB015941>

Received 10 APR 2018

Accepted 25 NOV 2018

Accepted article online 28 NOV 2018

Published online 8 JAN 2019

Influence of Clay, Calcareous Microfossils, and Organic Matter on the Nature and Diagenetic Evolution of Pore Systems in Mudstones

Eliza J. Mathia^{1,2}, Thomas F. T. Rexer^{1,3}, K. Mark Thomas⁴ , Leon Bowen⁵, and Andrew C. Aplin⁶

¹School of Natural and Environmental Sciences, Newcastle University, Newcastle upon Tyne, UK, ²Now at Chemostrat Ltd, Welshpool, UK, ³Now at Max Planck Institute for Dynamics of Complex Technical Systems, Magdeburg, Germany, ⁴School of Engineering, Newcastle University, Newcastle upon Tyne, UK, ⁵Department of Physics, Durham University, Science Laboratories, Durham, UK, ⁶Department of Earth Sciences, Durham University, Science Laboratories, Durham, UK

Abstract Mudstones exert a fundamental control on the flow of both aqueous and nonaqueous fluids in sedimentary basins. Predicting their flow and storage properties requires an understanding of pore size and connectivity, yet there are very few quantitative descriptions of pore systems of mineralogically and texturally well-characterized mudstones. We use a combination of electron microscopy, mercury injection capillary pressure porosimetry, and CO₂ sorption methods to generate a quantitative description of the size distribution, connectivity, and evolution of pore systems in a sequence of Posidonia Shale mudstones buried to 100–180 °C. We place the pore data into a detailed mineralogical, petrographical, and textural context to show that the nature and evolution of porosity and pore systems can be described in terms of associations with clay-rich, microfossil-rich, and organic matter-rich domains, common to many mudstones. Pore size distributions are described by power laws, and pore systems are well connected across the full nanometer-micrometer spectrum of pore sizes. However, connected networks occur primarily through pores <10 nm radius, with typically 20–40% of total porosity associated with pores with radii < ~3 nm, within both organic matter and the clay matrix. Clay-rich, microfossil-rich, and organic matter-rich domains have distinct pore size distributions which evolve in very different ways with increasing thermal maturity. We suggest that the flow of aqueous and nonaqueous fluids depends not only on the overall connectivity of pores but also the larger-scale connectivity and wetting state of clay-rich, microfossil-rich, and organic matter-rich domains.

Plain Language Summary Mudstones are Cinderella sediments: important but neglected. The most abundant sediment type, they act as unconventional oil and gas reservoirs, as top seals to conventional hydrocarbon reservoirs, and as critical barriers to the leakage of CO₂ and radionuclides from underground storage sites. Risking and predicting flow and leakage through these rocks requires a quantitative description of pore systems and their connectivity. This is challenging since even the biggest pores in shales are smaller than a micron, with many pores only a few nanometers in size. Our work uses a combination of techniques to characterize and quantify the nanoporous nature of shales. Pores are generally smaller than 100 nm but are well connected, but mainly through throats less than 20 nm. We have also placed the pore system data into a geological framework in order to be more predictive about the pore systems of shales generally. By quantifying the nature of pores in the various mineral and organic building blocks of shales we can consider the larger scale flow properties of shales and thus their potential either to transmit fluid (useful for a shale gas reservoir) or to retain fluid (useful for a CO₂ or nuclear waste storage site).

1. Introduction

Mudstones are the volumetrically most important sediment type and exert a fundamental control on the flow of both aqueous and nonaqueous fluids in sedimentary basins (e.g., Aplin & Macquaker, 2011; Nordgård Bolås et al., 2004; Schlömer & Krooss, 1997; Smith, 1971). They also act as unconventional oil and gas reservoirs, as seals to conventional hydrocarbon reservoirs, and as barriers to the leakage of CO₂ and radionuclides from underground storage sites.

Quantitative descriptions of pore systems underpin our understanding of the storage and flow of both aqueous and nonaqueous fluids in mudstones. Building a robust and predictive framework for the occurrence and development of mudstone pore systems requires consideration of three linked challenges. First,

©2018. The Authors.

This is an open access article under the terms of the Creative Commons Attribution-NonCommercial-NoDerivs License, which permits use and distribution in any medium, provided the original work is properly cited, the use is non-commercial and no modifications or adaptations are made.

mudstones are hugely diverse in terms of mineralogy, lithology, and texture, comprising complex assemblages of particles and particle aggregates derived from both extrabasinal and intrabasinal sources (e.g., Aplin & Macquaker, 2011; Milliken, 2014). This results in a wide range of minerals and particle types, of which the volumetrically most common classes are clay minerals, quartz and feldspar, biogenic carbonate, biogenic silica, and both terrestrial and marine organic matter (OM).

Second, burial diagenesis converts muds into mudstones through a range of mechanically and chemically driven processes which fundamentally alter both porosity and rock texture. Porosity declines from 80% at deposition to below 5% at depths of ~5 km. And the most volumetrically important components of mudstones—clay minerals, biogenic silica, biogenic carbonate, and OM—all undergo substantial chemical and textural changes during burial diagenesis (e.g., Aplin & Macquaker, 2011; Day-Stirrat et al., 2008, 2012; Hill, 1987; Hower et al., 1976; Isaacs, 1981; Milliken et al., 2012; Milliken & Olson, 2017).

Third, the characterization of the architecture of mudstone pore systems is technically challenging: Pores range in size from subnanometer to micrometer and single-measurement techniques rarely probe the complete size spectrum.

The combined challenge is thus to quantitatively describe the occurrence and evolution of mudstone pore systems as a function of (a) the original mineral and particle assemblage and (b) the mechanical and chemical modifications which occur during burial diagenesis. The diversity of mudstones makes this a substantial task but one which might be simplified by the individual consideration of the major mineralogical and lithological components of mudstones: for example, clay minerals, OM, biogenic carbonate, and biogenic silica. By emplacing quantitative pore size data into a petrographic and mineralogical context, this is the approach that we adopt in this paper.

Techniques used to investigate pore systems fall into three general categories: fluid invasion, neutron and X-ray scattering, and microscopy. While fluid invasion techniques such as gas sorption and mercury injection capillary pressure (MICP) porosimetry have been used for decades to characterize microporous to macroporous media (e.g., Conner et al., 1986; DeWit & Scholten, 1975; Diamond, 1970; Joyner et al., 1951; Zwietering & Koks 1954), they have rarely, until recently, been applied to mudstones (but see Borst, 1982; Schowalter, 1979). Similarly, small-angle neutron and X-ray scattering techniques have been used since the 1980s to characterize pore systems, with a few studies on mudstones suggesting a characteristic power law scattering behavior arising from a surface fractal pore structure with pores ranging in size from 2.5 nm to 2.5 μm (Clarkson et al., 2013; Hall et al., 1983, 1986; Mildner et al., 1986).

A limitation of these earlier studies is that they were rarely linked to a detailed description of mineralogy, texture, or maximum burial temperature. Petrographic methods are required to place fluid invasion and scattering data into a potentially predictive geological context. Technological developments in electron and He ion microscopy now allow pores down to ~10 nm (broad ion beam scanning electron microscopy [BIB-SEM] and focused ion beam scanning electron microscopy) and 1 nm (He ion microscopy) to be imaged and placed into a petrographic framework (Desbois et al., 2009; Houben et al., 2013; Klaver, Desbois, Littke, & Urai, 2012; Klaver, Desbois, Urai, & Littke, 2012; Klaver et al., 2015; Kliewer et al., 2012; Ko et al., 2017; Loucks et al., 2009; Mathia et al., 2016; Milliken & Curtis, 2016; Milliken et al., 2013; Pommer & Milliken, 2015; Wang et al., 2016). Furthermore, quantitative pore size distribution data can be extracted from scanning electron microscopy (SEM) methods, albeit with the key practical limitation that, over a representative elementary area (REA), pores smaller than ~50 nm diameter are underrepresented (Klaver, Desbois, Littke, & Urai, 2012; Klaver, Desbois, Urai, & Littke, 2012).

The drive to characterize and predict the pore systems of fine-grained sediments has increased markedly in the last decade because of their exploitation as major hydrocarbon reservoirs. Recent studies have used microscopy, MICP, gas sorption, and small-angle scattering techniques both alone and in combination to measure and infer aspects of pore structure and connectivity (e.g., Bernard et al., 2011, 2012, 2013; Chalmers & Bustin, 2012; Chalmers et al., 2012; Clarkson et al., 2013, 2016; Curtis et al., 2012; Klaver, Desbois, Littke, & Urai, 2012; Klaver, Desbois, Urai, & Littke, 2012; Ko et al., 2017; Fishman et al., 2012; King et al., 2015; Loucks et al., 2009; Mastalerz et al., 2013; Milliken et al., 2013; Modica & Lapierre, 2012; Ross & Bustin, 2009). These studies have started to unravel the nature of mudstone pore systems but have rarely quantified the pore architecture as a function of lithology, texture, and thermal maturity.

In this paper, SEM, MICP, and CO₂ sorption methods are combined to quantify the way in which nanometer- to micrometer-sized pore systems evolve as a function of mineralogy, texture, and maturity in a series of marine, OM-rich, calcareous mudstones from the Posidonia Shale in northern Germany (~100–180 °C; 0.53–1.45% vitrinite reflectance [Ro]). These samples are especially useful because previous studies have shown the similarity of the OM type and mineralogy of samples taken from three wells penetrating sequences of different maturity (e.g., Littke et al., 1991; Rullkötter et al., 1988; Vandenbroucke et al., 1993). Furthermore, in a previous paper Mathia et al. (2016) gave a detailed description of the petrography, mineralogy, and geochemistry of the samples, so that the pore system data presented in this paper have a detailed lithological context. We can therefore quantify the nature of pore systems associated specifically with the dominant clay-rich, carbonate-rich, and OM-rich components of the mudstones and show how each evolves as a function of thermal maturity. Because all three domains are common in many mudstones, we suggest that the results can be used more broadly to understand key controls of the storage and flow of both aqueous and nonaqueous fluids in mudstones.

2. Samples and Methodologies

The work reported here uses the same samples described in Mathia et al. (2016). Readers are referred to that paper for details about the location and burial history of the samples, along with detailed petrographic descriptions and the mineralogical and geochemical methods used to determine bulk sample properties. Those data, reported in Mathia et al. (2016), give essential context to the work reported here and are given in Tables 1–3. Further details of samples, along with the methods used to generate the new results reported here, are given below.

The Posidonia Shale of the Lower Saxony Basin, North Germany, is a calcareous mudstone deposited in an epicontinental sea during the Lower Toarcian, Jurassic (e.g., Littke et al., 1991; Röhl & Schmid-Röhl, 2005). It contains well-preserved, Type II marine OM with minor contributions of terrestrial macerals (Bour et al., 2007; Littke et al., 1991; Röhl et al., 2001).

Samples were taken from stratigraphically equivalent sections of three boreholes in the Hils syncline: Wickensen (WIC; 0.53% Ro), Harderode (HAR; 0.89% Ro), and Haddessen (HAD; 1.45% Ro). Twenty-six samples representing different stratigraphic units and maturities were selected for bulk analyses including Rock-Eval, total organic carbon (TOC), grain density, and total porosity. Most samples were taken from the lowest and highest maturity wells due to sample availability. To correct for an oil-in-kerogen peak, four mudstone samples were solvent extracted with a mixture of dichloromethane (93%) and methanol (7%) and subsequently analyzed for its remaining hydrocarbon potential. All the solvent-extracted samples had their grain densities remeasured. Changes in the measured grain density before and after solvent extraction enabled estimates of porosity occluded by soluble bitumen ($\varnothing_{\text{extractable_bit}}$) according to the following equation:

$$\varnothing_{\text{extractable_bit}} = \left(\frac{1}{\rho_g} - \frac{1}{\rho_{g \text{ ext}}} \right) \rho_g \quad (1)$$

where $\varnothing_{\text{extractable_bit}}$ (%) is the calculated porosity filled by extractable bitumen, ρ_g and $\rho_{g \text{ ext}}$ (g/cm³) are measured sample grain densities using the “Small Pycnometer Method” (Mathia et al., 2016), before and after solvent extraction, respectively.

The term $\varnothing_{\text{extractable_bit}}$ also includes porosity contained in pores with equivalent radii (in short radii) $< \sim 3$ nm ($\varnothing_{\text{extractable_bit_3nm}}$), quantitatively estimated by low-pressure CO₂ sorption experiments (see below).

Quantification of porosity filled by bitumen soluble in organic solvents allowed the estimation of true, soluble bitumen-free, total porosity:

$$\varnothing_{\text{tot_extractable_bit}} = \varnothing_{\text{tot}} + \varnothing_{\text{extractable_bit}} \quad (2)$$

where $\varnothing_{\text{tot_extractable_bit}}$ (%) is total porosity after solvent extraction of soluble bitumen, $\varnothing_{\text{extractable_bit}}$ (%) is the calculated porosity filled by extractable bitumen, and \varnothing_{tot} (%) is “as-received” total porosity. In addition, potential total porosity resulting from the conversion of kerogen to petroleum, the complete expulsion of petroleum, and zero mudstone compaction or cementation can be estimated by

Table 1

TOC-Normalized Mineralogical Composition (wt %) of Posidonia Shale for Wickensen (WIC; 0.53% Ro), Harderode (HAR; 0.89% Ro) and Haddessen (HAD; 1.45% Ro) Samples

Composition	WIC 7129	WIC 7135	WIC 7145	WIC 7147	WIC 7155	HAR 7038	HAR 7046	HAR 7060	HAR 7070	HAD 7083	HAD 7090	HAD 7110	HAD 7119
Quartz	12.4	15.1	11.8	14.0	7.8	14.6	16.4	12.2	10.8	11.1	14.8	14.1	7.6
Plagioclase	1.0	0.2	0.9	0.6	1.3	1.9	2.0	2.6	3.7	2.4	2.8	3.2	4.5
K-Feldspar	0.7	0.0	0.0	0.0	0.0	0.5	0.4	0.4	0.5	0.5	0.1	0.7	0.6
Calcite	32.4	35.8	41.5	38.1	50.0	40.1	39.5	28.7	42.2	49.5	36.8	28.5	46.3
Dolomite	0.3	0.0	0.3	0.2	0.5	0.6	1.0	6.0	2.0	0.6	1.7	3.7	2.5
Siderite/Ankerite	0.4	0.0	0.8	1.8	0.5	0.2	0.3	0.3	0.3	0.1	0.8	0.4	0.6
Aragonite	nd	nd	1.2	nd	1.2	nd	nd	nd	nd	nd	0.6	nd	1.4
Pyrite	4.8	4.5	3.5	3.7	4.9	5.2	4.8	8.6	5.2	6.9	4.6	6.6	4.2
Marcasite	0.7	nd	nd	nd	nd	0.6	0.2	0.9	1.2	nd	nd	0.2	nd
Anatase	0.3	0.1	nd	0.1	nd	0.3	0.2	0.2	0.3	0.2	nd	0.4	nd
Muscovite	2.3	2.2	0.0	1.2	0.1	2.9	2.8	3.5	3.0	2.4	1.2	4.4	0.0
Illite + I/S	21.7	22.0	20.0	25.4	17.5	17.0	18.9	24.7	18.3	13.3	22.1	23.5	18.1
Kaolinite	10.4	6.0	4.5	7.1	2.0	8.2	6.8	6.2	4.0	6.1	3.6	8.1	1.0
Dickite	nd	nd	1.1	nd	0.9	nd	nd	nd	nd	nd	1.2	nd	0.0
Chlorite	nd	0.4	1.8	0.2	1.6	nd	nd	nd	nd	0.0	0.6	nd	2.5
Gypsum	nd	0.3	2.0	0.4	2.2	nd	nd	nd	nd	0.4	1.7	nd	3.5
Halite	nd	0.1	nd	0	nd	nd	nd	nd	nd	0.1	nd	nd	nd
TOC	12.6	13.3	10.9	7.3	9.7	7.9	6.8	5.8	8.7	6.4	7.4	6.4	7.2
Total	100	100	100	100	100	100	100	100	100	100	100	100	100

Note. The TOC content (wt %) was determined with a LECO C-S analyzer. nd = not detected; TOC = total organic carbon.

$$\emptyset_{pot} = \emptyset_{original} + \emptyset_{OM_conversion} \quad (3)$$

where \emptyset_{pot} (%) is potential total porosity, $\emptyset_{original}$ (%) is original porosity in immature shale, and $\emptyset_{OM_conversion}$ (%) is porosity created due to thermal conversion of initially immature kerogen and complete expulsion of generated petroleum.

The last component of equation (3) can be estimated as a function of kerogen type, maturity, and initial TOC by calculating the proportion of OM that has been converted to petroleum and assuming complete expulsion of generated petroleum. The loss of organic carbon (wt %) for each maturity level was calculated according to Justwan and Dahl (2005) and Jarvie et al. (2007) and converted to volume percent OM following the approach of Coskey (2001).

Mercury injection data were collected with a Micrometrics Autopore II on samples previously freeze dried at -50°C and evacuated to 0.69 Pa. Total mudstone porosity was determined from grain density and bulk density when immersed in mercury at absolute pressure of 0.172 MPa. Pore sizes were calculated as a function of applied pressure according to the Washburn equation (Washburn, 1921) with the following input parameters: an advancing contact angle of 141° , a receding contact angle of 140° , and a surface tension of 0.485 N/m. The maximum pressure of 283 MPa generated pore radii data down to 3 nm. A full intrusion-extrusion cycle was run for selected samples with the final pressure decrease to 0.172 MPa.

Porosities and pore size distributions inferred from mercury injection data were corrected for large pores, interpreted to be artifacts resulting from destressing and drying (Figure 1). To estimate the radius of the onset of Hg intrusion into the true, in situ porous network of each sample, pore volume density data (Figure 1a) were compared with both cumulative mercury volume data (Figure 1b) and pore throat areas (Figure 1c). For the latter, calculated areas of pore throats cross-sectioned by a theoretical plane were grouped in size bins and plotted as a function of pore volume intruded by mercury (see Bernal & Bello, 2001; Houben et al., 2013):

$$\log\left(\frac{V_i}{b_i}\right) = -D \cdot \log(S_i) + \log C \quad (4)$$

where V_i is the volume of mercury intruded through pores with the characteristic area S_i within bin size b_i , C is a constant, and D is the power law exponent (Houben et al., 2013). For $i = 1$, the bin size is defined by $b_i = 1$

Table 2

TOC, RockEval and grain density measurements, wells Wickensen (WIC; 0.53% Ro), Harderode (HAR; 0.89% Ro), and Haddessen (HAD; 1.45% Ro)

Sample	TOC (wt %)	S1 (mg HC/g)	S2 (mg HC/g)	HI (mgHC/gTOC)	T_{\max} (°C)	Grain density (g/cm ³)	Grain density after solvent extraction (g/cm ³)
WIC 7129	12.59	3.02	90.25	717	427	2.254	2.236
WIC 7133	8.71	2.57	54.90	630	434	2.392	—
WIC 7135	13.27	4.62	84.63	638	427	2.249	—
WIC 7137	10.25	3.18	68.10	665	427	2.343	—
WIC 7139	9.36	2.81	64.95	694	428	2.375	—
WIC 7142	10.43	3.52	72.37	694	426	2.346	—
WIC 7145	10.92	4.18	72.03	660	425	2.331	—
WIC 7147	7.28	2.26	47.76	656	434	2.458	—
WIC 7151	14.75	5.85	89.61	608	429	2.236	—
WIC 7153	7.34	2.45	48.37	659	431	2.489	—
WIC 7155	9.67	3.87	69.41	718	428	2.361	—
HAR 7038	7.90	3.29	30.17	382	449	2.493	—
HAR 7046	6.75	2.93	26.03	386	450	2.526	—
HAR 7060	5.78	1.47	19.72	341	447	2.592	2.682
HAR 7070	8.71	2.26	31.27	359	449	2.463	2.533
HAD 7083	7.35	0.75	4.10	56	465	2.589	—
HAD 7090	7.41	0.94	4.16	56	463	2.572	—
HAD 7094	5.21	0.845	3.52	68	459	2.608	—
HAD 7097	5.40	0.75	3.15	58	458	2.609	—
HAD 7099	6.51	0.98	3.86	59	463	2.576	—
HAD 7101	5.88	0.92	3.1	53	457	2.624	—
HAD 7104	5.04	0.72	3.385	67	459	2.620	—
HAD 7105	5.85	0.77	3.28	56	461	2.621	—
HAD 7110	6.36	1.07	3.79	60	462	2.600	2.618
HAD 7115	6.49	1.12	3.80	59	460	2.614	—
HAD 7119	7.15	1.23	3.16	44	458	2.607	—

Note. TOC = total organic carbon; HI = Hydrogen Index; HC = Hydrocarbon.

and for $i > 1$, $b_i = 2 \cdot b_1 - 1$. The resulting power law distributions were fitted with two linear regression lines (Figure 1c). The line with the smaller negative slope, through the largest pores, was interpreted as describing artifact pores. Smaller pores, considered as real, are described by a regression line with a higher negative slope, reflecting an increasing pore volume density of progressively smaller pores. The “true” pores are generally 2, sometimes 3 orders of magnitude smaller than the maximum measured pore sizes (see also Comisky et al., 2011).

Low-pressure sorption experiments were performed on Intelligent Gravimetric Analyzers, supplied by Hiden Isochema Ltd., Warrington, UK. Samples were crushed to particle sizes between 500 and 1,180 μm , loaded in the Intelligent Gravimetric Analyzers (130–160 mg) and outgassed to a constant weight (typically for ~4 hr), at

<0.0001 Pa and 110 °C. CO₂ was injected stepwise up to the pressure of 0.1 MPa at a constant temperature of 195 K (dry ice/acetone bath) to obtain a subcritical CO₂ isotherm. All isotherms were run twice to ensure experimental repeatability, which was typically $\pm 1.5\%$ at 0.1 MPa. Sorption pore volumes (SPVs) were calculated from the maximum uptake at 0.1 MPa, assuming the CO₂ density of 1.177 g/cm³ (density of CO₂ at 216.6 K; Compressed Gas Association, 1990). Corresponding sorption porosities were determined using measured grain densities.

For microscopic studies, carbon-coated, polished thin sections were examined using a Hitachi SU-70 High Resolution Analytical SEM, equipped with an Oxford Instrument Energy Dispersive X-ray microanalysis system (INCA Energy 700). Samples were viewed in backscattered electron (BSE) mode using the YAG detector with the following conditions: 15–8 mm working distance, 15 keV accelerating voltage, 2–4 nA filament current. To reduce surface roughness prior to SEM imaging, selected samples were polished

Table 3

Rock-Eval Results After Solvent Extraction for Four Selected Samples, Wells Wickensen (WIC; 0.53% Ro), Harderode (HAR; 0.89% Ro), and Haddessen (HAD; 1.45% Ro)

Sample	S1 + S2a				S1/TOC (mg HC/g TOC)
	S2a (mg HC/g)	(mg HC/g)	As % TOC	S2b (mg HC/g)	
WIC 7129	10.4	13.20	10.5	79.89	104.8
HAR 7060	4.5	5.89	10.2	15.25	101.9
HAR 7070	3.5	5.71	6.6	27.79	65.6
HAD 7110	0.7	1.74	2.7	3.05	27.4

Note. S1 = Free bitumen; S2a = kerogen bound, solvent-extractable bitumen; S2b = pyrolyzable but not solvent-extractable organic matter; TOC = total organic carbon; HC = Hydrocarbon.

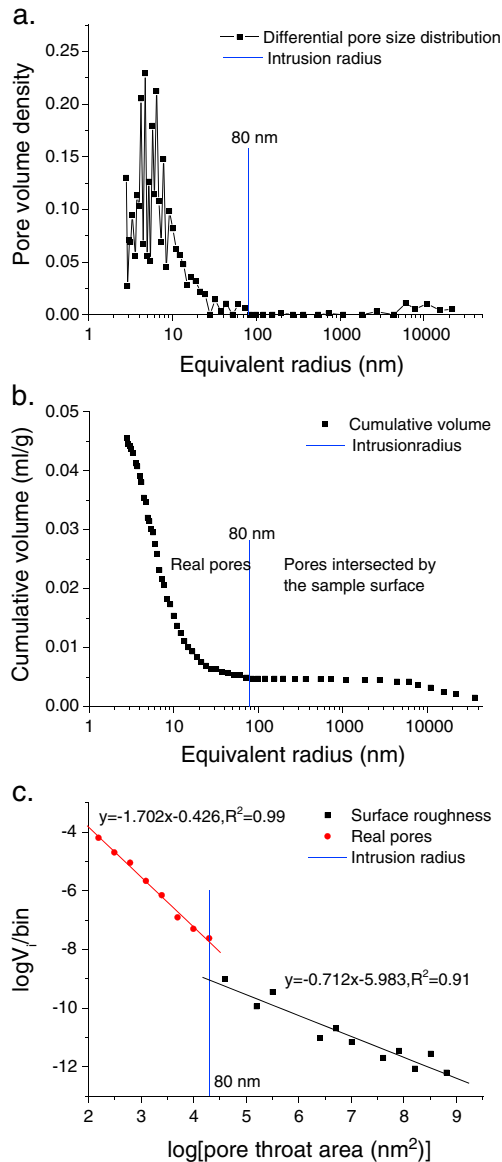


Figure 1. (a) Pore volume density and (b) cumulative volume of intruded mercury as a function of pore radius; (c) logarithm of pore volume within a size bin versus the logarithm of pore area. All plots are for sample WIC 7151 (0.53% Ro). Pores exhibit a nonuniform distribution with pores of >80-nm radius (gradient -0.712) interpreted as representing surface roughness and sample damage. Pores with <80-nm radius (gradient -1.7) are interpreted as true pores. WIC = Wickensen.

is greater. To account for unresolved pores and to determine the minimum, fully resolved pore size in the BIB-SEM mosaics, we used a method which assumes that the distribution of pore surfaces in 2-D is defined by a power law equation (see Houben et al., 2013; Klaver, Desbois, Littke, & Urai, 2012; Klaver, Desbois, Urai, & Littke, 2012):

$$\log[N_i] = -D \cdot \log[S_i] + \log[C] \quad (5)$$

where N_i is the number of pores with the characteristic surface area S_i , D is the power law exponent, and C is a constant of proportionality. A normalized, discrete distribution of surface area can then be used to compare the pore size data from different image mosaics using the equation

with an argon broad ion beam (BIB) in a Gatan 691 Precision Ion Polishing System (PIPS™). To fit into the PIPS™ chamber, the sample size was reduced to a 3-mm diameter disc with a Gatan 601 Ultrasound Disc Cutter, using a water emulsion of boron nitrate powder as a saw. The discs were bombarded with Ar ions in a vacuum (0.01 Pa) for 6 hr (angle 3°, 5 kV, 1–20 μA). Images were captured in the secondary electron mode using a through-the-lens detector at magnifications of 10,000X (pixel size 6 nm) and 6,000X (pixel size 15 nm), using the Automate mosaic building option. The choice of magnification was a compromise between the requirements of machine time and the time-consuming postanalysis of very small pores; this approach allowed us to quantify pores >25–50 nm in radius over larger sample areas. For selected mosaics, an energy dispersive X-ray (EDX) mode was implemented, generating maps of elemental and phase distribution. Microanalysis settings for the EDX collection were set at 300-μm dwell time, 15-kV accelerating voltage and 4-nA filament current. The areas covered by EDX mapping varied between 4,397 and 133,023 μm². The phase extraction procedure involved conversion of each X-ray map into an RGB color mode map, its binarization, and area quantification with ImageJ 1.44 software (Abramoff et al., 2004).

To determine a REA for estimations of image porosity, the modified box counting method described in Houben et al. (2013) was applied. In this method, continuous variations in a given property are measured over gradually increasing areas of investigation. We determined a REA using a mineralogical criterion. Elemental (SEM-EDX) maps were converted to mineral volumes and combined into four mineral groups: phyllosilicates, carbonates, quartz + feldspar, and pyrite. OM was excluded as it was largely unresolved in the EDX maps. Box counting was performed twice for each sample, starting from a point selected at random, and proceeded until the relative change in the content of a particular mineral group did not exceed 10% (Vandenbygaert & Protz, 1999).

For each representative mosaic, total image porosity was quantified by digitization of pore areas manually outlined in Adobe Photoshop 8.0. Digitization was followed by binarization and quantification using ImageJ 1.44 (Abramoff et al., 2004). For selected mosaics, OM content was quantified with a point counting method using JMicroVision 1.2.7 (Roudit, 2008). A minimum of 300 counts was made, until there was no significant change in the OM percentage. For one HAD sample, the fraction of porous and nonporous OM was additionally point-counted on two higher magnification (10,000X) image mosaics.

For a given magnification, there is a minimum pore size which can be visualized in the BIB-SEM image mosaics. At the 6,000X magnification used in this study, the pixel resolution is 15 nm and, since a group of pixels is required to define a pore, the minimum, fully resolved pore size,

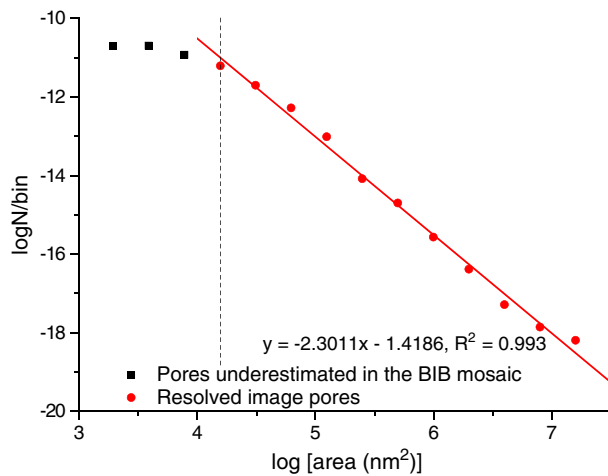


Figure 2. Logarithm of normalized frequency of pores as a function of the logarithm of binned pore area for pores segmented in an estimated representative elementary area ($96 \times 70 \mu\text{m}^2$) of the WIC 7129 sample. Fully resolved pores (red circles) are fitted with a linear regression line. Pores not fully resolved in image mosaics (black squares) deviate from the linear regression line. WIC = Wickensen.

$$\log\left(\frac{N_i}{b_i S_m}\right) = -D \cdot \log(S_i) + \log C \quad (6)$$

where N_i is the number of pores with the characteristic area S_i within bin size b_i , S_m is the surface area of the mosaic, C is a constant, and D is the power law exponent (Houben et al., 2013; Klaver, Desbois, Littke, & Urai, 2012; Klaver, Desbois, Urai, & Littke, 2012). For $i = 1$, the bin size is defined by $b_i = 1$ and for $i > 1$, $b_i = 2 \cdot b_{i-1} - 1$. The minimum pore size fully resolved in images is determined as the one corresponding to the minimum pore area that does not deviate from a straight line (Figure 2). Unresolved pore area (and thus unresolved porosity) between fully resolved pore size and a smaller, chosen pore size is estimated using the established power law relationship.

3. Results

3.1. Texture, Mineralogy, and Geochemistry

The bulk mineralogical composition of the sample suite is relatively constant throughout the whole maturity sequence, dominated by calcite and illite/smectite with lesser amounts of quartz, feldspar, dolomite, and pyrite (Table 1). Texturally, low maturity (WIC) samples are organic-rich, calcareous nannoplankton-bearing to calcareous nannoplankton-rich mudstones exhibiting macroscopically visible, millimeter-scale lamination delineated by different abundances of carbonate and clay components. Nanofossils, mainly intact or broken coccoliths, and disarticulated schizospheres, are the dominant calcitic component. The majority of nanofossils occur as debris concentrated in thin layers or as ellipsoidal aggregates—fecal pellets. In lighter laminae, nanofossil material tends to form continuous, $<50\text{-}\mu\text{m}$ -thick layers; in the dark laminae, isolated islands of fecal pellets are commonly surrounded by the clay-rich matrix (Mathia et al., 2016).

The intensity of carbonate chemical diagenesis increases with increasing maturity. In WIC samples, nanofossils are the most common form of calcite, with limited evidence for authigenic calcite. At higher maturities, nanofossil structures are lost and there are increasing amounts of authigenic calcite (Mathia et al., 2016). The loss of individual nanofossil structures suggests calcite dissolution and reprecipitation, but to provide specific textural evidence requires cathodoluminescence study. In SEM, we observed the presence of faceted calcite crystals in place of original coccoliths.

Kerogen is primarily Type II, and its maturation in this area has been studied previously (Table 2; Stock et al., 2017). Kerogen-bound but solvent extractable bitumen (S2a) consistently exceeds the amount of RockEval-measured free bitumen (S1) in WIC and HAR and is similar to S1 in HAD (Table 3). For the four solvent-extracted samples, the corrected Oil Saturation Index (S1/TOC) decreases from 105 mg/g TOC in WIC, to 66 and 102 mg/g TOC in HAR and 27 mg/g TOC in HAD.

The type and mode of occurrence of organic macerals change through the maturity sequence. In WIC, structured algal liptinite is the most common maceral but is less abundant than the microscopically unresolved, mineral-associated and strongly fluorescing matrix bituminite (Tao et al., 2012). In HAR, structured algal bodies are less abundant, either mechanically collapsed or filled with carbonate cement. The bituminous groundmass is much less fluorescent and instead, a dense network of nonsolvent extractable, solid bitumen fills pores within clay and fossiliferous domains. In HAD, no structured alginites are present, and a network of irregularly shaped, nonextractable, solid bitumen is a dominant feature. Solid bitumen fills microfractures, diagenetically altered fecal pellets, and spaces within clay aggregates.

3.2. Total Porosity

Total porosities, measured on as-received samples, change significantly with increasing maturity (Table 4 and Figure 3). In WIC samples, porosities range from 10% to 14%, declining to 2.5–4.5% in HAR. Porosities then increase to 9–14% in HAD samples. There is no relation between porosity and OM content at any maturity.

Table 4

Total Porosity, Mercury Injection Porosity and CO₂ Porosity, Wells Wickensen (WIC; 0.53% Ro), Harderode (HAR; 0.89% Ro), and Haddessen (HAD; 1.45% Ro)

Sample	Total porosity (%)	Mercury injection			CO ₂ at 195 K	
		Hg porosity (%)	Porosity <3 nm pore radius (%)	Hg ₉₀ pore radius (nm)	Sorption porosity (%)	Sorption pore volume (cm ³ /g)
WIC 7129	9.7	7.0	2.7	20	4.1	0.019
WIC 7133	12.8	9.5	3.3	26	—	—
WIC 7135	10.1	5.9	4.2	16	4.3	0.020
WIC 7137	10.6	8.1	2.5	16	—	—
WIC 7139	13.5	8.2	5.3	18	—	—
WIC 7142	12.2	8.4	3.8	22	—	—
WIC 7145	12.9	9.5	3.4	22	3.7	0.016
WIC 7147	11.4	10.4	1.0	34	3.6	0.015
WIC 7151	10.5	8.2	2.3	30	—	—
WIC 7153	13.9	11.2	2.7	60	—	—
WIC 7155	12.6	9.5	3.1	36	3.5	0.016
HAR 7038	3.1	1.3	1.8	10	2.0	0.008
HAR 7046	4.6	0.7	3.9	6	—	—
HAR 7060	4.5	2.0	2.5	12	2.1	0.008
HAR 7070	3.5	1.7	1.8	12	2.5	0.010
HAD 7083	13.7	10.4	3.3	28	3.8	0.015
HAD 7090	11.2	6.0	5.2	18	4.2	0.017
HAD 7094	12.1	8.2	3.9	20	3.9	0.016
HAD 7097	11.9	5.3	6.6	14	—	—
HAD 7099	10.6	3.2	7.4	8	—	—
HAD 7101	11.8	7.6	4.2	14	—	—
HAD 7104	11.6	4.6	7.0	10	—	—
HAD 7105	11.2	6.4	4.8	12	—	—
HAD 7110	9.4	3.5	5.9	10	3.8	0.015
HAD 7115	9.3	4.7	4.6	12	—	—
HAD 7119	11.3	8.3	3.0	30	3.3	0.013

Note. Hg₉₀ is the pore radius defining the 90th percentile of the cumulative pore size distribution.

In WIC and HAD samples, porosity correlates positively with calcite, and negatively with phyllosilicate content, but this is not seen in the small number of HAR samples (Figure 3).

Results from RockEval analysis and solvent extraction indicate the presence of soluble bitumen in all samples (Tables 2 and 3). Although not measured directly, porosity occluded by soluble bitumen $\varnothing_{extractable_bit}$ was estimated with equation (1) using changes in the measured grain density, and low-pressure sorption ($\varnothing_{extractable_bit_3nm}$ in pores <3 nm radius) before and after solvent extraction; this was done for four samples. Because there was no change in the measured grain density in the WIC sample before and after solvent extraction, we could not estimate the porosity filled by soluble bitumen. For the two HAR samples, soluble bitumen-filled porosity is estimated at 2.8% and 3.4% of total rock volume, and 0.7% in the HAD sample (Figure 4). Consequently, soluble bitumen-free porosities (equation (2)) are higher than those in as-received samples, amounting to 6.3–7.8% (compared to 3.5–4.5%) in HAR samples and 10.1% (compared to 9.4%) in the HAD sample.

During source rock maturation, kerogen is converted to petroleum and some or most of the generated petroleum is expelled (Burnham & Braun, 1990); as a result, porosities would increase if the rock structure was incompressible and no petroleum was retained in the rock structure. In this case, we suggest that at each maturity stage, potential total porosity would consist of the following components (Figure 4):

$$\varnothing_{pot} = \varnothing_{tot} + \varnothing_{extractable_bit} + \varnothing_{lost} \quad (7)$$

where \varnothing_{pot} (%) is potential total porosity, \varnothing_{tot} (%) is as-received total porosity, $\varnothing_{extractable_bit}$ (%) is the calculated porosity filled by extractable bitumen not expelled from the rock, and \varnothing_{lost} (%) is porosity lost in a sample due to compaction of the rock structure and/or formation of solid bitumen. To calculate \varnothing_{lost} , we first solved equation (3) by estimating the potential newly created porosity ($\varnothing_{OM_conversion}$) as a function of

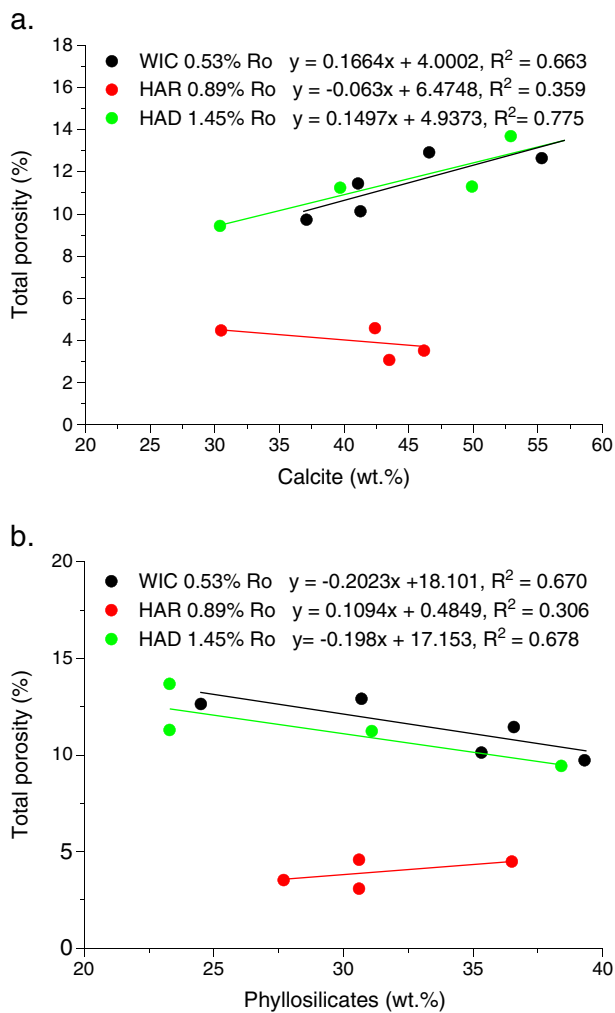


Figure 3. Total porosity versus X-ray diffraction-determined weight percent of (a) calcite and (b) phyllosilicates for Wickensen (WIC), Harderode (HAR), and Haddessen (HAD) samples.

and the pore throats that connect them (Webb, 2001). When pore bodies are larger than pore throats, pores will be emptied of mercury at capillary pressures lower than the corresponding intrusion pressures, and some mercury will remain trapped in pore bodies (Padhy et al., 2007). Figure 6c shows the difference between porosity intruded and emptied during intrusion-extrusion experiments at equivalent pressures, as a function of pore radius. Very little mercury is drained at high capillary pressures, equivalent to pores smaller than 10–20 nm radius. For pore radii greater than 17 and 13 nm for WIC and HAD samples, respectively, the rate of extrusion exceeds the rate of intrusion at equivalent pressures, and mercury starts to recede from the small pores that could not be emptied previously. The curves show that 90% of porosity is not emptied until extrusion pressures decrease to pressures corresponding to the 10–20 nm threshold radius. An alternative interpretation links the strength of the hysteresis and the mercury extrusion rate to the amount of OM. Mathia (2015) showed that the maximum percentage of porosity that is not emptied at equivalent intrusion pressures decreases linearly with increasing TOC. This suggests that compression of the shale structure may take place during mercury porosimetry experiments (Friesen & Mikula, 1988), especially for organic-rich shales.

3.4. CO₂ Sorption Porosity

Carbon dioxide isotherms for both as-received and solvent-extracted mudstones at 195 K do not reach plateaus and are therefore classified as Type I/II in the IUPAC Classification Scheme (Figure 7; Sing et al., 1985). The sorption isotherm at 195 K is measured close to the CO₂ saturation limit and provides a gas adsorption

kerogen type, maturity and initial TOC, and assuming an original porosity at 10% (Table 4), typical for immature WIC shale ($\phi_{original}$). The calculated transformation ratios of the Posidonia kerogen, representing the proportion of the petroleum potential which has been generated, are as follows: 5% for WIC 7129, 63% for HAR 7060, 73% for HAR 7070, and 96% for HAD 7110. Theoretical porosity created due to thermal conversion of OM ($\phi_{OM_conversion}$; including potential OM-hosted pores) until the completion of each maturity stage, is then 0.8% in WIC, 7–8% in HAR, and 13% in HAD. Finally, porosity lost (ϕ_{lost}) due to compaction and the occurrence of solid bitumen is 0.8% for WIC7129, 9.0% for HAR7060, 11.9% for HAR7070, and 12.7% for HAD7110 (Figure 4). Lost porosity in HAR exceeds porosity that was previously created due to OM loss ($\phi_{OM_conversion}$). In consequence, when directly comparing measured as-received total porosities (ϕ_{tot}), a porosity loss of around 7%, or around 4% if pore-filling, soluble bitumen is accounted for, occurs between WIC and HAR. In contrast, the calculated, newly created porosity between HAR and HAD, 5% of rock volume, is similar to that measured experimentally.

3.3. Mercury Injection Porosity

In our experiments, the smallest pore throats injected by mercury have 3-nm radius. Pores larger than this and accessible to mercury represent 60–90% of total porosity in WIC, typically 40–50% in HAR and typically 40–75% of total porosity in HAD (Table 4). Hg_{90} , defined here as the 90th percentile of the cumulative pore throat size distribution, ranges from 3 to 30 nm radius, and is less than 15 nm in all but three samples (Table 4). There is no clear relationship between mineralogy and pore size distribution; the smallest pore throats and the narrowest pore size distributions occur in the oil window (HAR) samples (Figure 5).

Mercury extrusion experiments were performed on one WIC and one HAD sample (HAR was omitted due to low sample availability). There is a very striking intrusion-extrusion hysteresis and the majority of injected Hg is retained at the end of the experiment (Figures 6a and 6b). There is continuing debate about the meaning of these experiments and the extent to which the results reflect sample compressibility and/or the nature of the pore system (e.g., Suuberg et al., 1995; Toda & Toyoda, 1972). One interpretation is that the hysteresis reflects differences in the size of pore bodies

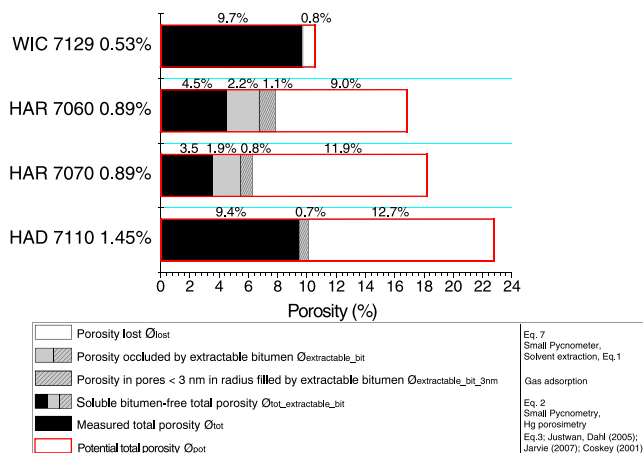


Figure 4. Potential total porosity (red outline) based on initial porosity and loss of organic matter during thermal maturation, for WIC 7129 (0.53% Ro), HAR 7060, HAR 7070 (0.89% Ro), and HAD 7110 (1.45% Ro). Potential total porosity is the sum of experimentally measured total porosity in “as received samples” (black bars), porosity occluded by solvent extractable bitumen (gray bars), including in pores of <3-nm radius (gray dashed bars), and porosity lost due to mudstone structure compaction/cementation and/or retention of now solid bitumen (white bars). For each maturity step, potential total porosity was calculated as the sum of the initial porosity before the onset of hydrocarbon generation (here 10% porosity, typical of WIC samples), and porosity created during thermal conversion of organic matter, assuming (a) 100% efficient petroleum expulsion and (b) zero compaction and cementation. The method of measurement or estimation of each type of porosity is listed on the bottom right. WIC = Wickensen; HAR = Harderode; HAD = Haddessen.

total pore volume. All SPV were calculated from the adsorbed volume at $P/P_0 = 1$, assuming an adsorbed phase density of 1.177 g/cm^3 (density of CO_2 at 216.6 K; Compressed Gas Association, 1990), and range between 0.008 and $0.020 \text{ cm}^3/\text{g}$ (Table 4). As for both total, and mercury injection porosity, SPVs and porosities are lower in HAR than WIC and HAD. Sorption porosity correlates positively with TOC in WIC but not in HAD (Figure 8a). Only a weak relationship was found between SPV and the combined TOC plus clay content (soft component) in WIC (Figure 8b). The limited number of HAR samples precludes any clear relationships between sorption porosity and mineralogy.

The sorption isotherms shape (Figure 7) indicate evidence of microporosity (pores <1 nm radius) filled at the lowest pressures, as well as larger pores. We note that the sum of mercury injection porosity and CO_2 sorption porosity is similar to total porosity (Table 4), from which we infer that the 195 K sorption porosity is mainly that contained within pores with radii smaller than $\sim 3 \text{ nm}$ (see also Rexer et al., 2014). The combined porosities measured by CO_2 adsorption and mercury porosimetry account for virtually all the porosity.

CO_2 isotherms were additionally measured on four solvent-extracted samples. In all experiments, more CO_2 was adsorbed by the solvent-extracted samples (Figure 7b), resulting in an increase in the calculated sorption porosities at all maturities. For HAR and HAD samples, the calculated sorption porosity occluded by the extractable bitumen is between 0.8% and 1.1% of the rock volume (Figure 4), constituting 25–35% of the measured oil-free sorption porosity in the oil window, and 17% of the oil-free sorption porosity in the gas window sample. Consequently, sorption pores hold 31–33 vol % of the extractable oil calculated with equation (1) in the HAR mudstone, while in HAD, sorption pores hold all the extractable bitumen.

3.5. Porosity Observed by Electron Microscopy

3.5.1. REA

One sample from each maturity level (WIC 7129, HAR 7060, and HAD 7110) was selected for detailed electron microscopic analysis. The three samples are mineralogically similar (Table 5) but are texturally distinct, mainly because of diagenetic changes: higher maturity mudstones show lesser amounts of biogenic calcite and a more pronounced presence of large, diagenetically modified, nanofossil-rich aggregates.

In all three samples, mineralogically defined REA were determined to be areas close to $6,000 \mu\text{m}^2$; this is the area over which pores were counted and measured in this paper (Table 5). Recall that while mineralogy is used here to define REA, texture is another factor that is likely to exert an important control on pore systems.

3.5.2. Pore Size Distributions of REAs

Pore types were point counted on REAs with a pixel size of 15 nm. For the low-maturity mudstone, quantification was made on a macroscopically visible light lamina. All pores resolved on images were classified based on their spatial relation with respect to mineral phases and OM, using the classification of Loucks et al. (2012). We adapted the following definitions of pore types:

- Interparticle.** (1) pores between detrital grains, authigenic minerals, nanofossils and clay flakes; and (2) pores (in 2-D or 3-D space) associated with the interface of OM and mineral matrix that visibly do not extend into an organic particle;
- Intraparticle.** (1) pores within single mineral grains or fossil bodies; (2) pores within well-defined fecal pellets and pyrite framboids; (3) moldic pores formed due to dissolution of mineral phases; and (4) pores at the interface of the inorganic matrix and organic macerals that do not extend into an organic particle, contained within a fossil body, fecal pellet or pyrite framboid;
- Organic.** (1) discrete, round, bubble-like pores in the OM; (2) sponge-like pores within the OM, often interconnected and grouped; (3) irregularly shaped pores, often at the interface of the OM and mineral matrix,

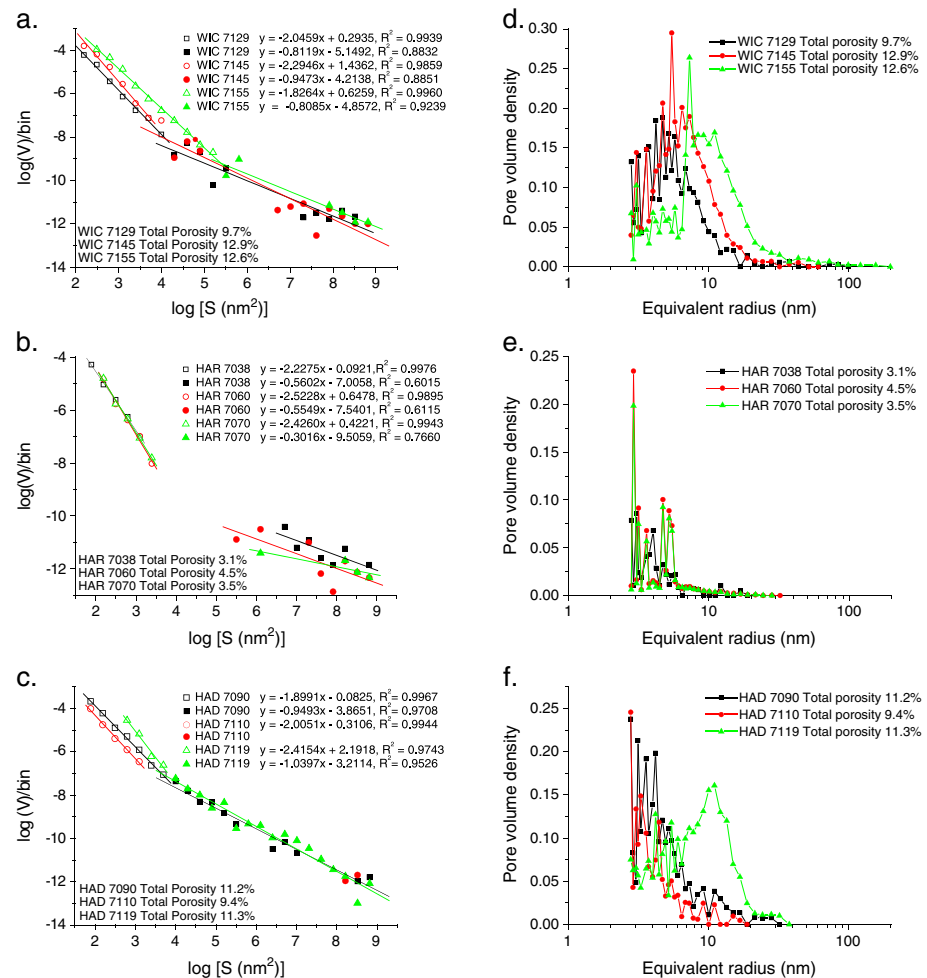


Figure 5. (a, b, c) Logarithmic of mercury injection pore volume (V) in size bins as a function of the logarithm of pore area (S) in selected Posidonia samples: wells Wickensen (WIC; 0.53% Ro), Harderode (HAR; 0.89% Ro), and Haddessen (HAD; 1.45% Ro). Regression lines through large pore areas are characterized by a low negative gradient (> -1.1) and are interpreted as surface roughness and pores due to sample damage. Regression lines with a high negative slope (< -1.8) describe real pores intruded by mercury. (d, e, f) Pore volume density distribution of real pores. The mercury data were cut off at a radius interpreted as the onset of intrusion into the naturally occurring pore network. This corresponds to the pore radius at which the two regression lines meet in panels a–c.

extending into the organic mass; and (4) visible cracks within OM particles, often with jagged edges and extending into the organic mass. Additionally, all organic pores that are fully contained within OM are subclassified as intraorganic pores; this distinguishes pores which have a size and shape unlimited by the surrounding mineral matrix.

Pore network types change through the maturity sequence from exclusively interparticle and intraparticle in WIC (47% and 53% of interparticle and intraparticle pores, respectively), to interparticle- and intraparticle-dominated in HAR (44% and 43%, respectively), and finally to interparticle and intraparticle-rich with a moderate proportion of organic pores in HAD (36%, 40%, and 24%, respectively; Table 6). In WIC, mineral-hosted porosity is associated mainly with aggregates of biogenic calcite (Figures 9a–9f). Pores also occur at the interface of mineral phases and OM, within pyrite framboids (Figure 9b), and are occasionally lined with organic material. In HAR, slit-shaped pores occur at the interface of the OM and mineral matrix, mainly found within calcite domains (Figures 10a and 10b); small amounts of porosity are present within pyrite framboids (Figures 10c and 10d), and within OM as cracks and fractures. In HAD, most of the visible pores are associated with calcite and pyrite (Figures 11a–11d). Pores hosted by OM are discrete, spongy and irregular (Figures 11c–11f), and interface pores are more common than at lower maturities.

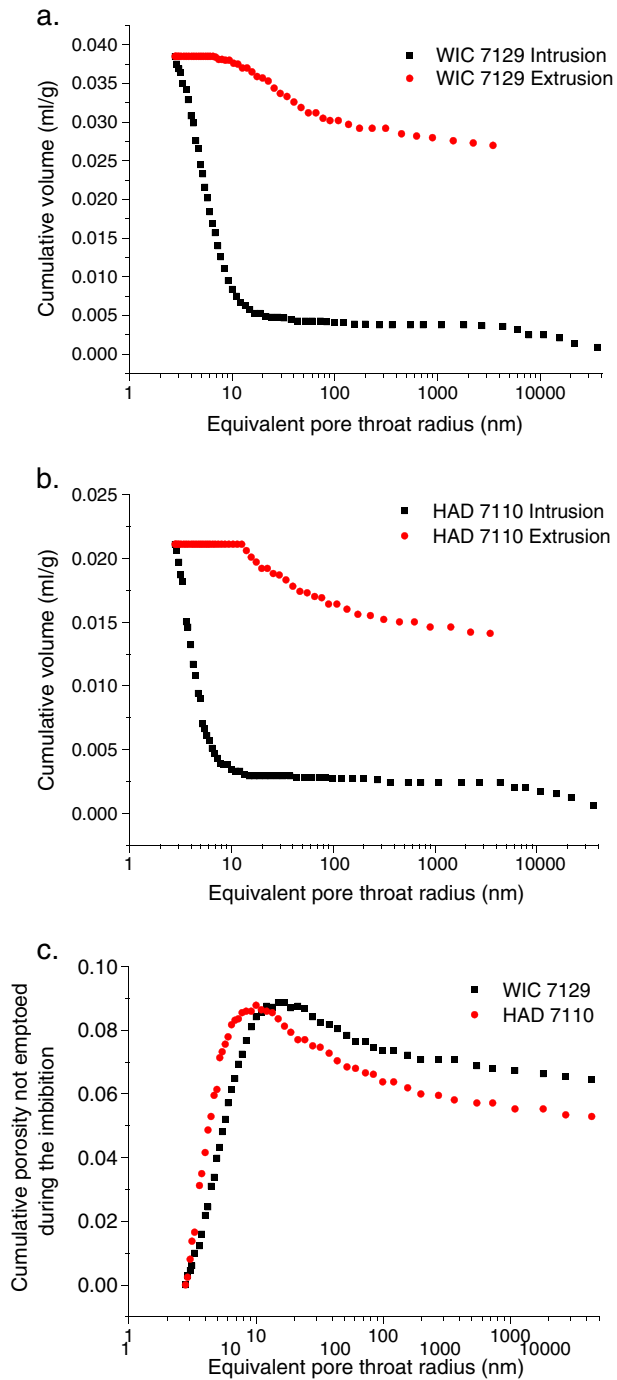


Figure 6. Cumulative intrusion (black) and extrusion (red) mercury injection curves for (a) WIC 7129 and (b) HAD 7110. (c) Cumulative porosity that is not emptied from mercury during the imbibition from the WIC 7129 (black) and HAD 7110 (red) samples. The curves plot differences between porosity intruded and emptied during the intrusion-extrusion experiments at equivalent pressures, as percent of the bulk sample. For pores with a radius <17 nm for WIC and <13 nm for HAD, the rate of extrusion is less than the rate of intrusion and thus a fraction of mercury is trapped. For pores with a radius >17 nm for WIC and >13 nm for HAD the rate of extrusion exceeds the rate of intrusion, implying that mercury is being drained from pores but at lower pressures than the corresponding intrusion pressures. WIC = Wickensen; HAR = Harderode; HAD = Haddessen.

Image extraction and binarization of the visible pores provide information about porosity, pore shapes, pore sizes, and pore size distributions. At all maturities, the distributions of fully resolved pores can be described by power laws with slopes of -2.30 in WIC, -2.34 in HAD to -2.50 in HAR (Figure 12a). As pores smaller than 50 nm radius could not be linearly fitted by these power laws, 50 nm is taken to be the minimum pore radius fully resolved in our REA images (Figure 2).

The resolved image porosity is similar in samples at all three levels of maturity: 0.7% in the light lamina of the WIC mudstone, and 0.6% and 1.1% in HAR and HAD, corresponding to 7%, 13%, and 12%, respectively, of the total porosity (Table 6). Although the median radius of resolved pores is 75–80 nm in all three samples (Figure 13a), aspect ratios of pores in HAR are on average twice those in the WIC and HAD (Figure 13b). This reflects the occurrence of pores at the interface of OM and inorganic matter (see Milliken et al., 2013).

In all three samples, there is an increase in frequency of pores with progressively smaller radii (Figure 13a). On the other hand, differential distributions of pore sizes show a single maximum located between 140 and 200 nm radius in WIC and HAD and 100–140 nm radius in HAR (Figure 12b). We investigated the factors which determine the position of this maximum by quantifying pores from four additional mosaics (Figures 9c, 10c, 11c, and 11e) over an area smaller than the REA, using a 10,000X magnification with a practical image resolution of 25 nm radius. Figure 12c shows that for the WIC sample, pore sizes in the darker, more clay-rich lamina, are skewed toward smaller radii compared to those in the lighter, more carbonate-rich lamina. In HAR and HAD, the original laminated texture is obliterated and the pore size distributions in different sample areas are similar.

At magnifications of 6,000X, the majority of resolved image porosity lies within inorganic domains, so that the size distribution of visible pores approximates that of mineral-hosted pores. However, this does not include pores potentially associated with clays, as those remained unresolved in all samples. Similarly, little is known about intraorganic pores, which due to their small sizes (radii <150 nm) account for only 17% of the image porosity in the HAD mudstone at a magnification of 10,000X (Table 6). To gather information about the size distribution of pores contained exclusively within organic particles, specific size distribution curves were constructed with all nonorganic porosity excluded. The resolved organic pores show a fractal distribution with a slope of -2.7 down to a pore radius 25 nm (Figure 12d). In contrast to the inorganic material-hosted pores, the differential pore size distribution of resolved, intraorganic pores shows no maximum; pores of decreasing size contribute progressively more porosity (Figure 12e).

Fully resolved image porosities, representing pores >50 nm radius in the REA mosaics, constitute only 7%, 13%, and 12% of total porosity in WIC, HAR and HAD samples, respectively. Comparison of image- and mercury injection-derived cumulative and incremental porosity curves show that the imaged pore bodies are 1–3 orders of magnitude larger than pore throats probed by the mercury injection experiments. This implies that, with no pore connections visible in images, the >50 nm radius pore bodies are either unconnected or are only connected through pore throats with radii typically smaller than 10–20 nm and “seen” by mercury (Figures 14a

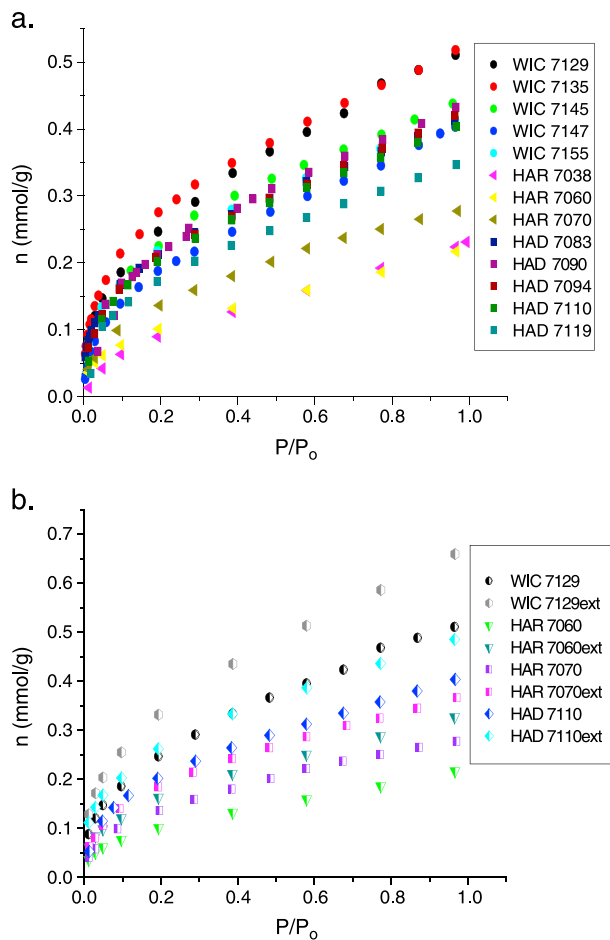


Figure 7. (a) CO₂ isotherms at 195 K on a relative pressure (P/P_0) basis for selected WIC 0.53% Ro (circles), HAR 0.89% Ro (triangles), and HAD 1.45% Ro (squares) mudstones. The x axis represents the relative pressure, and the y axis represents concentration (mmol/g) of CO₂ adsorbed at the temperature of 195 K. Samples were not solvent extracted prior to analysis. Peak oil window mudstones (HAR) show lower concentrations of adsorbed CO₂ than early oil window (WIC) and gas window (HAD) counterparts. (b) CO₂ 195 K isotherms for 7129 WIC 0.53% Ro (circles), 7060 HAR 0.89% Ro (triangles), 7070 HAR 0.89% Ro (squares), and 7110 HAD 1.45% Ro (diamonds) mudstone samples measured prior to and after solvent extraction (ext). Extracted mudstones show higher concentrations of adsorbed CO₂ than their nonextracted counterparts, at all maturities. WIC = Wickensen; HAR = Harderode; HAD = Haddessen.

and 14b). This is consistent with the differential distributions of image-resolved pores, which show decreasing contributions to porosity of pores smaller than 100–150 nm radius, down to the image resolution of 50 nm radius (Figure 12b).

Due to the limited resolution of the mosaics, we found no quantitative evidence for connectivity between image-resolved intraorganic pores, or their direct connectivity with mineral-hosted pores. However, if we assume a similar fractal behavior of the resolved and unresolved intraorganic pores (Figure 14c), we can extrapolate the log pore area-log pore number relationship and explore the importance of smaller pores. We extrapolated to 3 nm pore radius because this corresponds to the maximum pore volume density in the mercury-derived, differential pore size distribution curve (Figure 5f). These results show that if the unresolved, intraorganic pores follow the same size distribution as resolved pores, intraorganic pores would contribute 1.7–3.1% bulk porosity over the pore radius range 3–150 nm (Table 6). This represents 18–33% of the total porosity in HAD and would give an average porosity of OM of 24%.

Figure 14d shows cumulative porosity as a function of pore radius measured by (a) mercury injection and (b) image analysis in the HAD sample. Image analysis porosity combines imaged >50 nm radius pores and intraorganic pores extrapolated down to 3 nm radius (see above). Porosities determined by each method are similar, suggesting that intraorganic pores could account for all the mercury-measured porosity observed between 3 (our extrapolation limit and mercury resolution in this study) and 20 nm radius (typically the maximum radius of pore throats seen by mercury). In this gas window sample, these intraorganic pores could thus form a connected pore network.

3.5.3. Distribution of Image Porosity in Microdomains

Higher-resolution image mosaics allow investigation of pores in relation to mineral phases and micro-domains. Pores were counted on 130 images of the three different maturity samples using a 10,000X magnification. This corresponds to a pixel size of 6 nm and an effective minimum pore radius of 25 nm – the smallest macropore size. Calcite, phyllosilicates, pyrite, and OM were also estimated from EDX data, allowing the image porosity to be related to these components. Results are shown in Figure 15.

As clay packages are not porous in SEM images (Figures 9–11), there is no correlation between EDX-derived phyllosilicate content and image porosity, at any maturity (Figure 15a). Similarly, no correlation was found for pyrite, despite the porous nature of pyrite framboids in the highest maturity sample; this simply reflects the fact that pyrite is not a volumetrically significant phase.

The relationship between image porosity and calcite is important and changes substantially as a function of maturity (Figures 15b–15d). In WIC, we differentiated between porosity imaged in the clay-enriched (darker) and calcite-enriched (lighter) laminae. In both cases, image porosity increases slightly with calcite content (Figure 15b). The most striking observation is that there are some regions, exclusively within lighter laminae, that have higher image porosities (3–6%). Petrographic observations suggest that these are areas where biogenic calcite has been more pervasively converted to authigenic calcite.

Light and dark laminae cannot be differentiated in HAR and micrographs were classified into two groups depending on the content of fecal pellets. Fecal pellet-rich domains include areas dominated by calcite aggregates of biogenic origin, with a strong diagenetic overprint. Matrix-rich domains comprise areas rich in clays, quartz, pyrite framboids, and only discrete carbonate crystals. Figure 15c shows that in HAR,

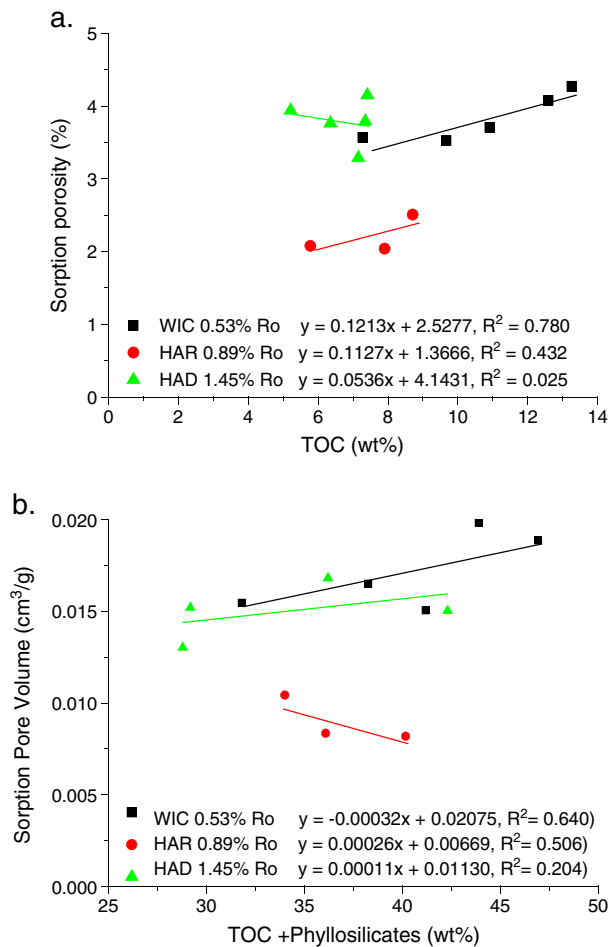


Figure 8. (a) Sorption porosity versus weight percent TOC in WIC 0.53% Ro, HAR 0.89% Ro, and HAD 1.45% Ro mudstones. (b) Sorption pore volume versus weight percent total organic carbon plus phyllosilicates. TOC = total organic carbon; WIC = Wickensen; HAR = Harderode; HAD = Haddessen.

(e.g., Jarvie et al., 2007; Modica & Lapierre, 2012; Figure 4; see Milliken & Olson, 2017, for a general discussion of porosity loss and generation in mudstones). In fact, measured porosities of 10–14% in immature samples decrease to 3–5% in the oil window and then increase to 9–14% into the gas window (Figure 3). The porosity decrease into the oil window can be partly explained by the retention of solvent-extractable OM, which accounts for 30–40% of the porosity decrease. The rest of the measured porosity decrease must be due to one or both of (a) compaction and (b) retention of nonextractable bitumen in the pore system. There are two important implications of these results; firstly, compactional loss of porosity will lead to an increase in fluid pressure and will be a key driver for petroleum expulsion; secondly, retained bitumen becomes a locus

image porosities are 0–1.5% and are not strongly related to calcite content; higher porosities (>0.6%) are always associated with fecal pellet domains.

The clearest relationship between image porosity and calcite occurs in HAD (Figure 15d). Micrographs and associated porosity were divided into fecal pellet- and matrix-rich domains. Fecal pellet-rich domains are characterized by higher calcite contents and exhibit higher porosities (3–7%) than the matrix domains (0.3–3%). Image porosities in the fecal pellet domains in HAD are up to an order of magnitude greater than image porosities found in both matrix and fecal pellet domains in HAR; they are generally higher than image porosities in both light and dark laminae in WIC.

Since OM in both WIC and HAR contains very few macropores, there is no relationship between visible porosity and OM at these maturities (Figures 15e and 15f). In HAD, the fecal pellet domains are generally rich in OM (>20%) and, for a given OM content, have higher image porosities than other domains (3–7% compared to 1–3%; Figure 15g). However, most of the image porosity in both matrix and fecal pellet domains is *not* intraorganic, with intraorganic porosity ranging from 0% to 0.5%, almost independent of domain (Figure 15h). Image porosity thus increases from oil window to gas window, especially in the fecal pellet-rich domains, but most of the generated macroporosity is not *within* the organic phase.

The sum of point-counted image porosity and OM is plotted as a function of calcite content in Figure 16. In the absence of compaction and cementation, the conversion of solid organic material to petroleum, coupled to petroleum expulsion, would generate porosity, and the sum of OM plus porosity would remain constant. Figure 16 shows that the sum of image porosity and OM is similar in HAR and HAD samples, but lower than those observed in WIC.

4. Discussion

4.1. Evolution of Total Porosity

If these organic-rich rocks were incompressible through the maturation sequence, significant porosity would be generated because of the loss of kerogen and the concomitant generation and expulsion of petroleum

Table 5

Comparison of Bulk Mineralogical Composition (vol %) Estimated with EDX on a Representative Elementary Area (REA) and Measured by XRD

Phase Method	Phyllosilicates (vol %)		Quartz + feldspar (vol %)		Carbonates (vol %)		Pyrite (vol %)	
	EDX	XRD	EDX	XRD	EDX	XRD	EDX	XRD
WIC 7129	24 ± 4	26.0	6 ± 3	10.9	30 ± 6	24.8	3 ± 1	2.0
HAR 7060	35 ± 3	31.5	10 ± 4	14.3	32 ± 9	31.6	4 ± 2	4.2
HAD 7110	37 ± 7	31.5	11 ± 3	16.1	30 ± 10	28.0	4 ± 1	3.1

Note. XRD mineral contents (wt %) were converted to volume % using standard grain densities of minerals. EDX = energy dispersive X-ray; XRD = X-ray diffraction; WIC = Wickensen; HAR = Harderode; HAD = Haddessen.

Table 6

Binarized BIB-SEM Image Porosities and Point-Counted Relative Contributions of Different Pore Types in Selected Posidonia Shale Samples: WIC 7129 (0.53% Ro), HAR 7060 (0.89% Ro), and HAD 7110 (1.45% Ro)

Sample	Area (μm^2)	BIB image porosity (%)	BIB image porosity as fraction of total porosity	Intraorganic porosity extrapolated to a pore radius 3 nm (%)	Intraorganic porosity (>3 nm radius) as fraction of total porosity	Percent of interparticle, intraparticle, and organic pores
WIC 7129	96 × 70	0.7	0.07	—	—	47-53-0
HAR 7060	96 × 70	0.6	0.13	—	—	44-43-13
HAD 7110	96 × 70	1.1	0.12	—	—	36-40-24
HAD 7110 Intraorganic	153 × 96	0.2	0.02	1.7–3.1	0.18–0.33	—

Note. The minimum fully resolved pore radius is 50 nm, except for the intraorganic pores of the HAD sample, where it is 25 nm. BIB-SEM = broad ion beam scanning electron microscopy.

for porosity generation during subsequent burial and gasification (e.g., Bernard et al., 2012; Ko et al., 2017; Mathia et al., 2016; Milliken et al., 2013; Pommer & Milliken, 2015).

Porosity generation between 0.89% and 1.45% Ro shows that the loss of biogenic calcite and the related development of authigenic calcite, does not result in significant compaction of the organo-mineral matrix. Around 40% of the observed porosity increase can be explained by the loss of extractable bitumen, presumably through expulsion, with 60% attributable to the thermal decomposition of pyrolyzable OM. The latter is inferred from the agreement between the increase in bitumen-free total porosity, and the amount of calculated new porosity that would be created between 0.89% and 1.45% Ro (Figure 4). The increase in porosity from decomposition of OM is also consistent with the reduction in the RockEval S2. We suggest that in the oil window, pore-filling, nonextractable bitumen must form part of this S2 peak, and is therefore volumetrically significant (Behar et al., 2008; Lewan, 1997; Michelis et al., 1996; Wilhelms et al., 1990).

It is now well-established that a microporous to macroporous pore system is developed within the OM of mudstones as a result of gas generation (e.g., Bernard et al., 2012; Loucks et al., 2009; Milliken et al., 2013; Rexer et al., 2014). Some (e.g., Jarvie et al., 2007; Modica & Lapierre, 2012) have suggested that the total volume of new porosity can be estimated purely as a function of the initial OM content and the extent to which the OM has been converted to fluids, which are subsequently expelled. The porosity reconstructions in this work show that this is not the case, but that information is also needed about both compaction and the amount of extractable and nonextractable bitumen trapped within pores in the oil window.

4.2. Porosity Distribution Within Clay-, Carbonate-, and OM-Rich Domains

Combined mineralogical and petrographic data indicate that porosity in these samples can be considered in terms of its association with carbonate-rich, clay-rich and OM-rich domains, the three main components of Posidonia mudstones (Figures 3, 8–11, and 15). Figure 3 shows the positive relationship between porosity and calcite and the related inverse relationship between porosity and phyllosilicates, with the same trend observed in WIC and HAD samples (HAD does not fall on the same trend and will be discussed separately). These trends imply that some porosity is associated with calcite-rich domains. However, extrapolation of the trend to 0% calcite suggests an excess porosity of around 4%, which we interpret as being at least partly clay-associated; this represents 30–50% of total porosity.

Although clay-associated pores have been imaged with high resolution SEM and TEM in these and other mudstones (e.g., Fishman et al., 2012; Houben et al., 2013, 2014; Klaver, Desbois, Littke, & Urai, 2012; Klaver, Desbois, Urai, & Littke, 2012; Mathia et al., 2016), no clay-associated porosity was observed at the magnifications of 6,000X and 10,000X used in this study. However, only ~10% of total porosity can be resolved at these magnifications. Figure 8 shows that there is a moderate correlation between the pore volume probed by CO₂ sorption and the sum of OM plus phyllosilicates, in both WIC and HAD. Since (a) the sum of CO₂ sorption porosity plus mercury injection porosity is close to the total porosity, and (b) mercury intrudes pores to a minimum radius of around 3 nm, we infer that most of the CO₂ sorption porosity is within pores with radii smaller than 3 nm. Detailed work by Rexer et al. (2014) showed that around half the CO₂ sorption volume in Posidonia

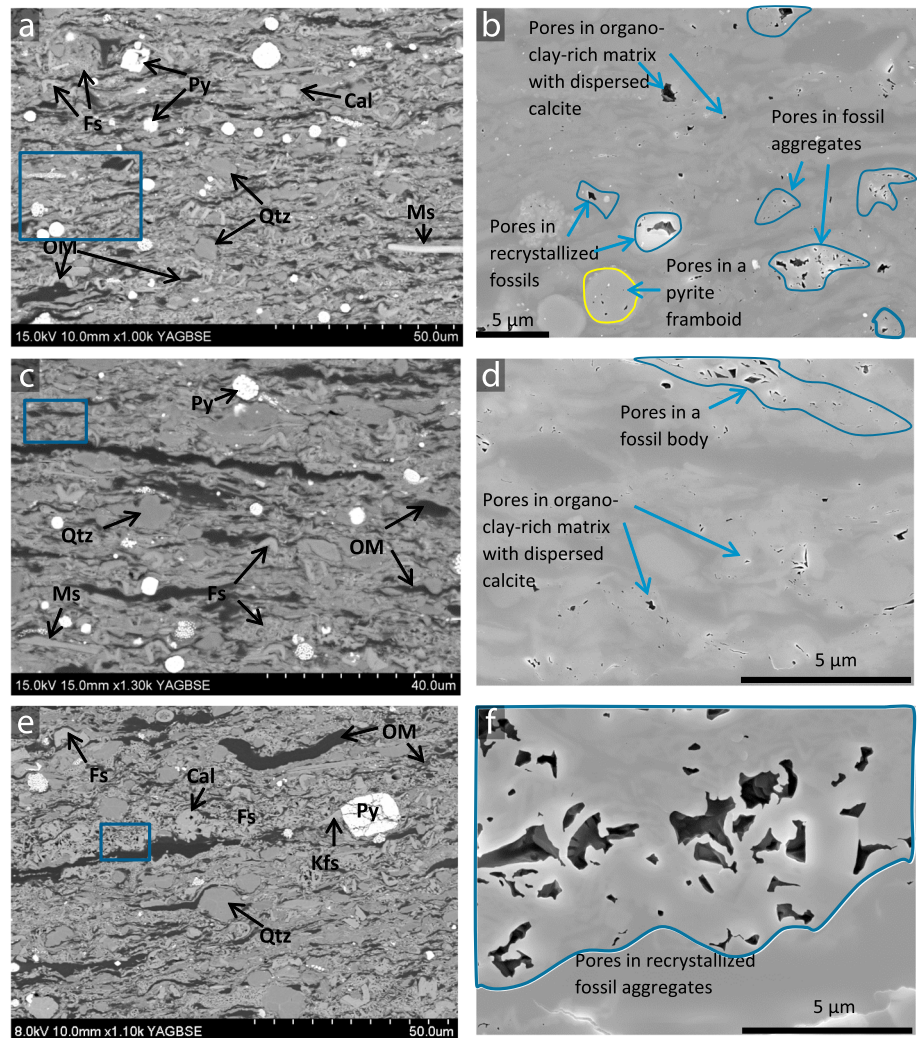


Figure 9. BSE micrographs (left column) of WIC 7129 mudstone samples polished with the argon broad ion beam. Secondary electron micrographs (right column) show details of porosity distribution within areas outlined with a blue rectangle in BSE micrographs. The bedding plane in all images is horizontal. (a) Calcareous mudstone (light lamina) with disseminated fecal pellets alternating with clay material, silt-size quartz, pyrite framboids, and sparsely disseminated calcite. (b) Pores are found within fossil aggregates, locally within pyrite framboids, and in the organoclay-rich matrix with dispersed fossils. (c) Calcareous mudstone (dark lamina) enriched in the clay material admixed with organic matter, with disseminated silt-size quartz, pyrite framboids, and calcite fossils. (d) Pores dispersed in an organoclay + calcite matrix and in fossil bodies. (e) Calcareous mudstone (light lamina) with recrystallized fossiliferous aggregates alternating with organic matter-rich and clay-rich laminae. (f) Pores in diagenetically modified fossil aggregates can reach 3 μm in diameter. Note lack of organic material lining the pores. BSE = backscattered electron; WIC = Wickensen; Py = pyrite; Fs = fossil; OM = organic matter; Qtz = quartz; Ms = muscovite; Cal = calcite; Kfs = K feldspar.

mudstones was associated with OM, implying that the rest was within the phyllosilicate matrix. Furthermore, MICP data indicate that the clear majority of pore throats in all samples have radii less than 10 nm (Figure 5). Combining these observations, we infer that there is substantial porosity associated with the clay matrix, and that pore radii are generally smaller than 10 nm.

While driven by different processes, the evolution of porosity in carbonate-rich and OM-rich domains are inter-related. In contrast to clay-rich domains, pores within the rigid calcareous matrix can be imaged in the REAs at all maturities. Visible pores range from 25 to 2,500 nm radius, with most pores smaller than 200 nm (Figure 12c). In immature samples, carbonate-associated pores are often within microfossil tests. With increasing maturity, calcite is dissolved and reprecipitated so that biogenic forms of calcite are

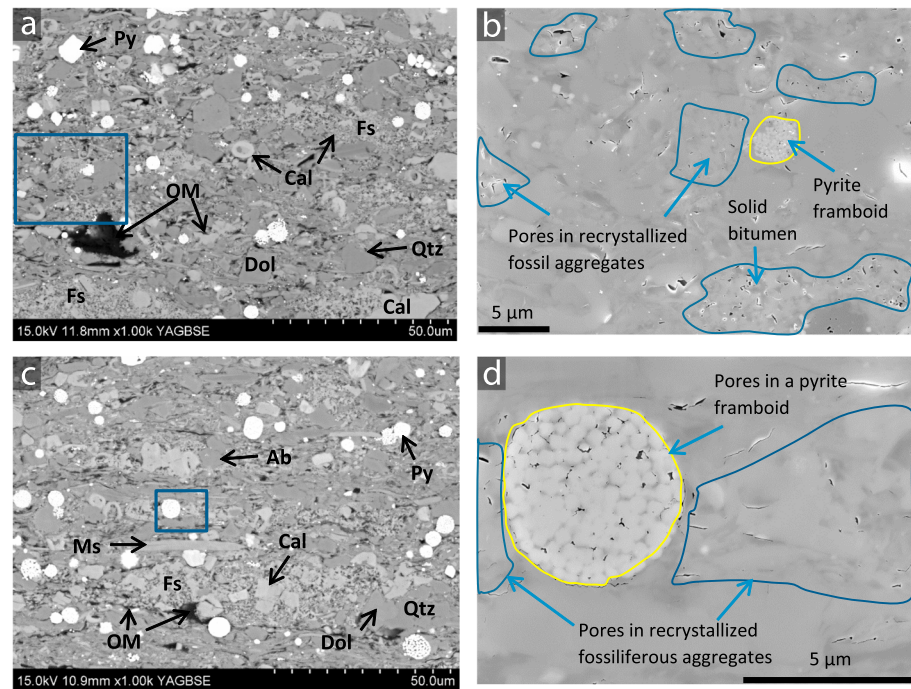


Figure 10. BSE micrographs (left column) of HAR 7060 mudstone samples polished with the argon broad ion beam. Secondary electron micrographs (right column) show details of porosity distribution within areas outlined with a blue rectangle in BSE micrographs. The bedding plane in all images is horizontal. (a) Calcareous mudstone with densely packed nanofossil aggregates. Partial recrystallization of the nanofossil-rich mudstone matrix and presence of calcite and dolomite cement all indicate diagenetic transformation of the original biogenic material. (b) Pores in recrystallized fossil aggregates occur at the interface with organic matter filling the intragranular space. (c) Calcareous mudstone with alternating calcite and clay laminae. Fossiliferous aggregates are to a large extent recrystallized and locally cemented. (d) Pores occur within fossiliferous aggregates as well as within pyrite framboids. BSE = backscattered electron; HAR = Harderode; Py = pyrite; Fs = fossil; OM = organic matter; Qtz = quartz; Ms = muscovite; Cal = calcite; Dol = dolomite; Ab = albite.

converted to authigenic calcite (Figures 9–11). There is no evidence that porosity is lost during carbonate diagenesis, suggesting that the development of contact cement arrests compaction and leads to the growth of larger pores at the expense of smaller pores.

Porosity is lost in the oil window, partly because of compaction (see Figure 6d in Mathia et al., 2016) but significantly because it is filled with both extractable and nonextractable bitumen. The clearest location of the pore-filling OM is within coccolith-rich fecal pellets, which act as micro-traps for migrating petroleum (Leythaeuser et al., 1988; Pommer & Milliken, 2015). Image porosity is thus very low in the oil window compared to immature samples, where much of the imaged porosity is associated with fossiliferous carbonate (Figures 15b and 15c).

Localized dissolution of biogenic calcite and its reprecipitation as authigenic calcite occurs coevally with petroleum generation and local trapping. We suggest that this process forms structurally rigid zones which inhibit further compactional porosity loss, most clearly within coccolith-rich fecal pellets. These structurally rigid zones are critical for the generation of secondary porosity resulting from both the expulsion of light petroleum and the generation of gas from trapped bitumen (Bernard et al., 2011, 2012). Within the gas window, image porosity, that is, pores with radii greater than 25–50 nm, is much greater in fecal pellets than in the general matrix (Figure 15d). Although only 25% of this porosity is OM-hosted, the increased porosity resulting from gas generation relates directly to the loss of OM from structurally rigid domains, previously filled with bitumen. This is supported by the observation that the average combined area of image pores plus OM, does not change between peak oil window to gas window (HAR to HAD; Figure 16).

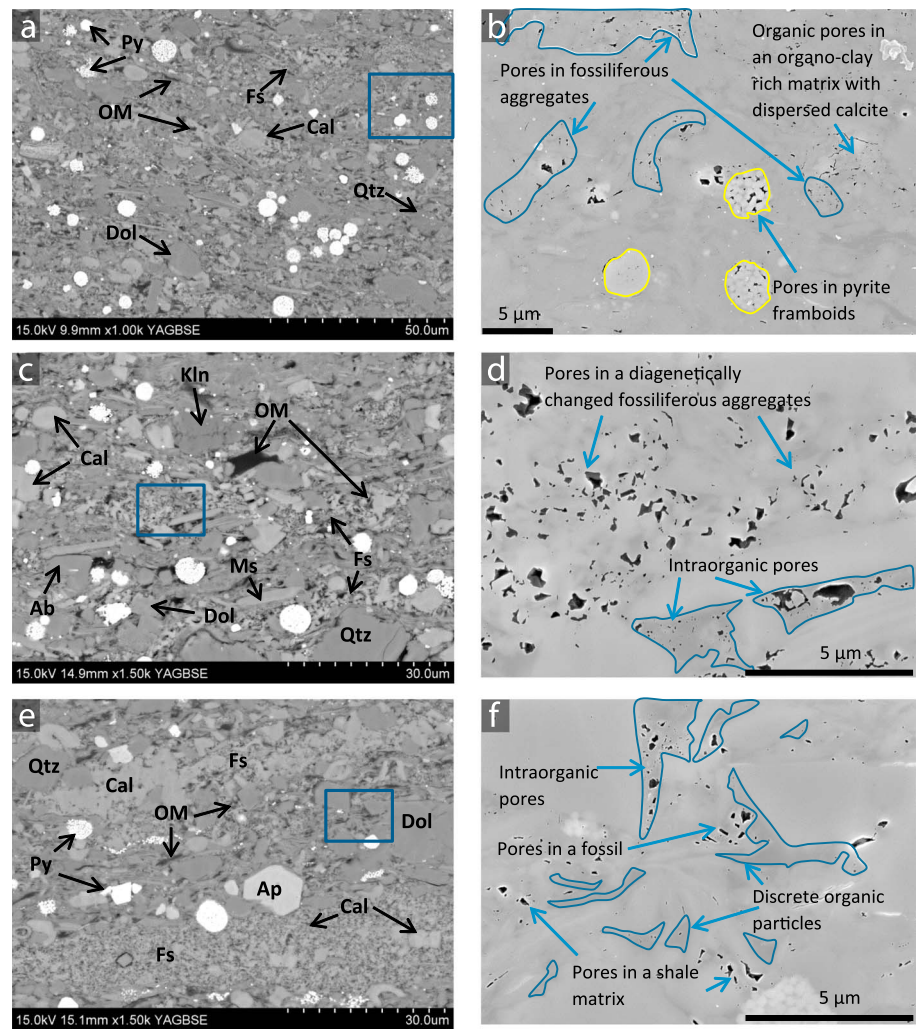


Figure 11. BSE micrographs (left column) of HAD 7110 mudstone samples polished with the argon broad ion beam. Secondary electron micrographs (right column) show details of porosity distribution within areas outlined with a blue rectangle in BSE micrographs. The bedding plane in all images is horizontal. (a) Calcareous mudstone with recrystallized fossils and authigenic carbonate phases. (b) Porosity occurs between crystallites in pyrite framboids, within well-defined, diagenetically modified fossiliferous aggregates as well as within-mudstone matrix. (c) Calcareous mudstone with a strong diagenetic overprint. (d) Common porous zones include fossiliferous aggregates and organic particles. (e) Common diagenetic features include recrystallized biogenic calcite in fecal pellets (top and bottom), and calcite cement. Dolomite replaces the original fabric. (f) Organic matter (outlined) ranges from nonporous to highly porous. BSE = backscattered electron; HAD = Haddessen; Py = pyrite; Fs = fossil; OM = organic matter; Qtz = quartz; Ms = muscovite; Cal = calcite; Ab = albite; Ap = apatite; Dol = dolomite; Kln = kaolinite.

4.3. Nature and Evolution of Pore Systems

The pore systems of the mudstones in this study are well-connected based on the observation that the sum of porosities measured by two fluid invasion techniques—CO₂ sorption and mercury injection—is similar to total porosity, in all samples. Since CO₂ and mercury probe pores with radius < ~3 nm and > ~3 nm, respectively (Rexer et al., 2014), this implies connectivity across the full pore size distribution. We now consider the nature of pore connectivity in the context of mineralogy and texture.

The clay matrix comprises 20–30 vol % of these samples and the combined image, CO₂ sorption and mercury injection data all suggest that clay-associated pores are smaller than 10–15 nm radius, with a substantial fraction <5 nm. These results are similar to Klaver, Desbois, Littke, and Urai's (2012) and Klaver, Desbois, Urai, and Littke's (2012) observations in immature *Posidonia* mudstones and consistent with Keller et al. (2013) and

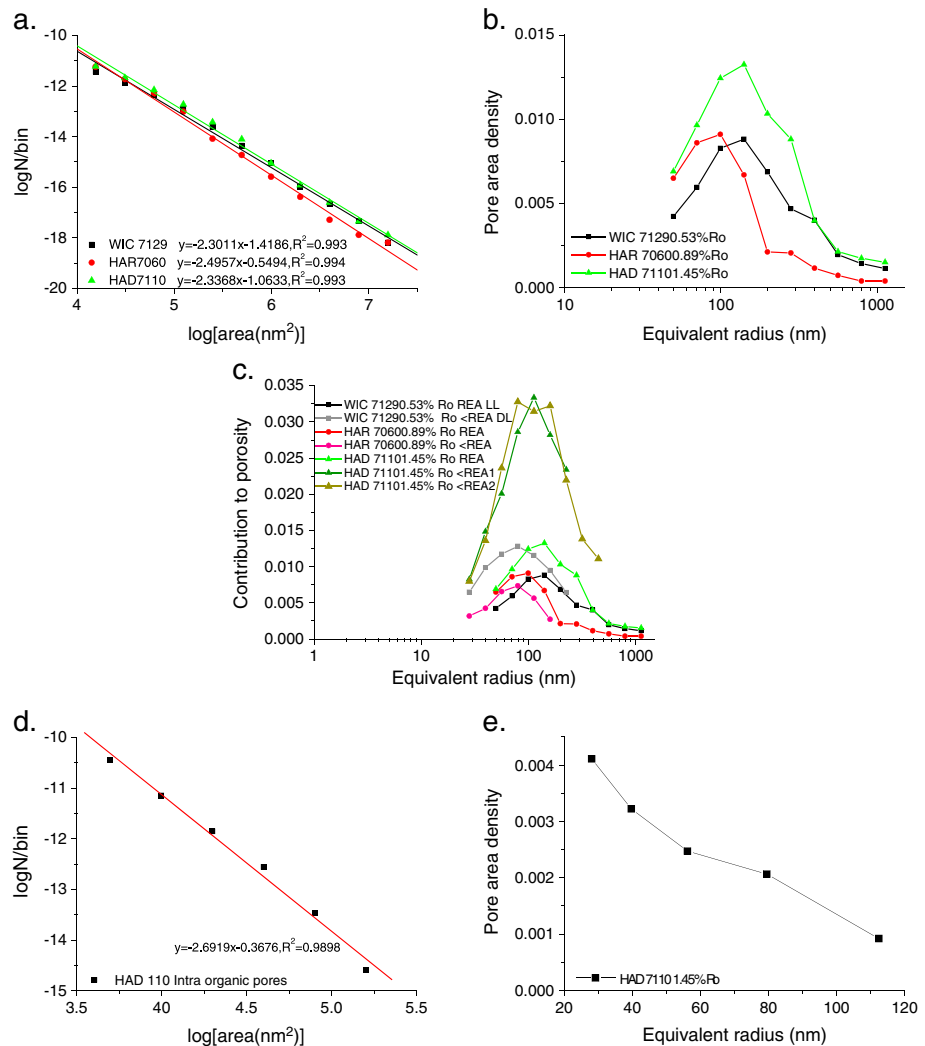


Figure 12. Pore size data from BIB-SEM images for three samples: WIC 7129 0.53% Ro, HAR 7060 0.89% Ro, and HAD 7110 1.45% Ro. (a) Logarithm of number of pores per bin versus pore area for pores >50 nm in radius, demonstrating a power law distribution. Note that porosity in pores with radius >50 nm approximates inorganic material-hosted porosity in all samples. (b) Differential pore size distribution as a function of an equivalent pore radius. Note descending pore area density of pores <200 nm radius. Data in (b) were captured from images at a 6,000X magnification with the fully resolved pore radius >50 nm and cover an estimated REA. (c) Differential pore size distribution as a function of an equivalent pore radius. These additional image mosaics were captured at a 10,000X magnification (<REA, resolved pore radius >25 nm). The WIC images were acquired in both light (LL) and dark laminae (DL). (d) Logarithm of number of pores per bin versus pore area for intraorganic pores >25 nm in radius for the HAD 7110 1.45% Ro mudstone. The BIB-SEM images were captured at a magnification of 10,000X, covering a full REA. (e) Differential pore size distribution of intraorganic pores as a function of equivalent pore radius. Note increasing pore area density toward smaller pore sizes. BIB-SEM = broad ion beam scanning electron microscopy; WIC = Wickensen; HAR = Harderode; HAD = Haddessen; REA = representative elementary area.

Song et al.'s (2016) data from the clay-rich Opalinus Clay, who both observed that the main connectivity between clay-related pores occurred on the ~10-nm scale.

Ten to 15% of total porosity is imaged in the REA and occurs in pores with radii greater than 50 nm. At all maturities, most of this porosity is associated with the carbonate matrix; in immature samples, this is primarily within microfossil tests and coccolith-rich fecal pellets, which become filled with migrated bitumen in the oil window. Into the gas window, dissolution and reprecipitation of carbonate results in a rigid matrix in which large pores can be formed and retained because of continuing expulsion of petroleum, and the densification

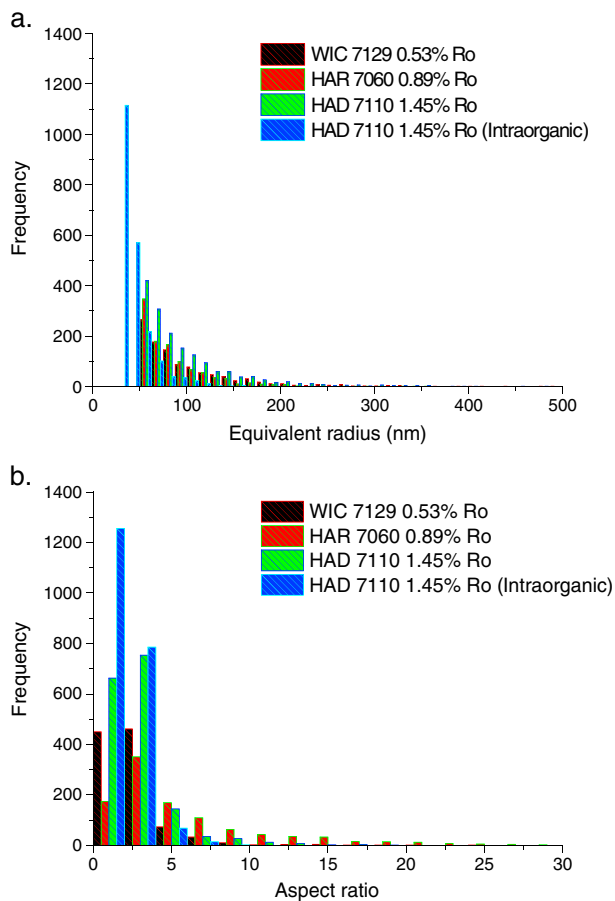


Figure 13. Distribution of (a) equivalent radii and (b) aspect ratios of BIB-SEM image pores for WIC 7129 0.53% Ro, HAR 7060 0.89% Ro, and HAD 7110 1.45% Ro. The histograms represent pores with a diameter above the practical image resolution. The magnification of a single image is 6,000X for histograms representing all pores and 10,000X for a histogram representing intraorganic pores only. BIB-SEM = broad ion beam scanning electron microscopy; WIC = Wickensen; HAR = Harderode; HAD = Haddessen.

of decreasing size contribute increasing amounts of porosity in pores from >100 nm down to 25 nm radius, the smallest visually resolved pores in this study (Figure 12e). If the fractal distribution of pore radii continues to 3 nm, which is consistent with small-angle scattering data from other mudstones (Clarkson et al., 2013; King et al., 2015) and is the minimum pore size accessed in the mercury injection experiments, then the extrapolated image porosity is very similar to the mercury injection porosity (Figure 14d). Intraorganic porosity then accounts for around 25% of the total porosity in the sample and suggests an average porosity of OM of 24%. Additional intraorganic porosity is also within pores smaller than 3 nm radius (Rexer et al., 2014). It appears that OM within the gas window has a fractal distribution of pores with the largest intraorganic pores (>25–100 nm radius) connected via a network of pores which increase in number and total volume with decreasing pore size. This can provide a viable transport pathway for gas within the mudstone *if* the organic phase is connected on a larger scale. Kuo et al. (1995) suggested that uniformly distributed OM networks lose 3-D connectivity when the TOC contents fall below 6 wt %. These Posidonia mudstones generally contain >6 wt % TOC (Table 1) and so may have a well-connected organic network.

4.4. Implications for Fluid Flow

The permeability of an organic pore network dominated by pores connected at diameters of say 20 nm will be around 10 nD (e.g., Yang & Aplin, 1998, 2007). Since OM comprises only 10 vol % of the rock, the permeability related to the organic network, expressed in terms of a bulk rock permeability, would thus be on the

and gasification of retained OM (Bernard et al., 2012, 2013; Mathia et al., 2016; Milliken et al., 2013; Modica & Lapierre, 2012; Pommer & Milliken, 2015).

The modal pore radius observed in images of the REA is around 100–200 nm, with sharply lower volumes in pores declining in size from 100–200 to 25–50 nm (Figure 12). Since only 10–15% of total porosity is in pores >50 nm radius, this suggests that these larger pores are connected only through much smaller pores. This is supported by mercury injection data, which imply that the vast majority of pore throats have radii of <10 nm (Figure 5). Similarly, the strong hysteresis between mercury intrusion and extrusion curves (Figure 6) is consistent with a system of relatively rare, large pores connected through a system of pores mainly <10 nm radius. Based on CO₂ sorption and MICP data, this includes a substantial amount of porosity within pores with radii smaller than ~3 nm, which comprises 10–40% of porosity in immature (WIC) samples, 50–80% in oil-window (HAR) samples and 25–70% porosity in gas-window (HAD) samples (Table 4).

OM in WIC and HAR samples contains no pores with radii >25 nm. OM is however microporous at all maturities, as shown by both high-pressure CH₄ and low-pressure CO₂ sorption data on kerogens isolated from the same samples as those analyzed here (Rexer et al., 2014). Approximately half the CO₂ sorption porosity is lost into the oil window, which we infer relates to (a) the reduction in the amount of OM because of generation and expulsion, and (b) the saturation of kerogen with generated bitumen (Table 4). This is supported by the observation that at all maturities, CO₂ sorption volumes increase by around 30% after solvent extraction (Figure 7). We infer that micropores and small mesopores are generated in overmature samples since the CO₂ sorption volumes in these samples are similar to those in immature samples, despite the fact that the OM contents have halved. Similar conclusions were reached by King et al. (2015) using a combination of small-angle scattering and He ion microscopy.

Intraorganic pores >25 nm radius only comprise 2% of the total porosity in the HAD mudstones (Table 6). However, in contrast to the total pore size distribution, which is dominated by inorganic pores, intraorganic pores

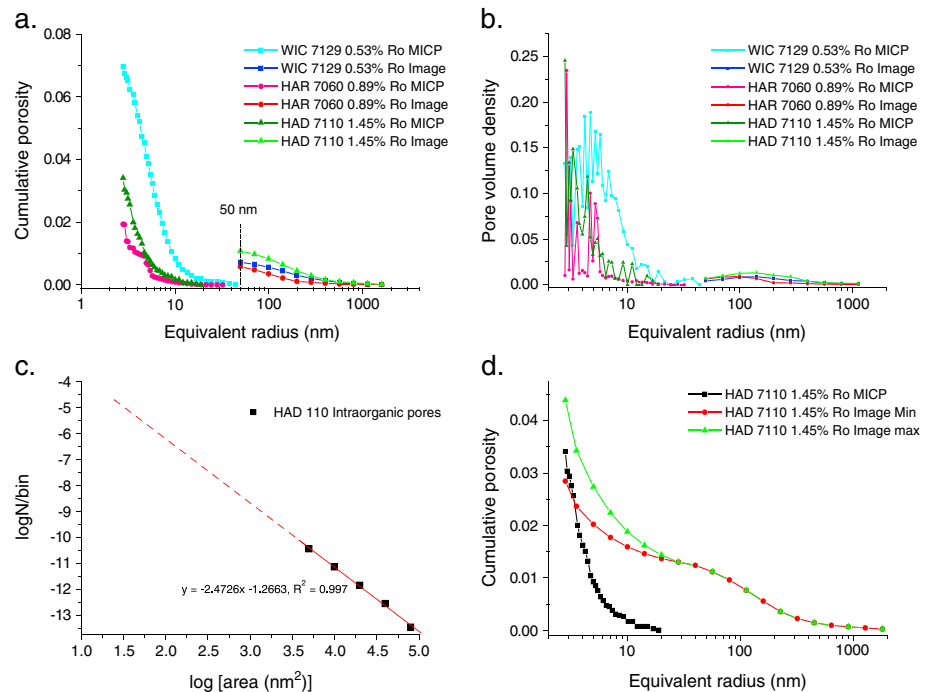


Figure 14. Comparison of (a) cumulative porosity and (b) pore size distribution obtained from mercury injection (pores >3 nm radius) and image analysis (>50 nm radius) covering the representative elementary area for three samples: WIC 7129 0.53% Ro, HAR 7060 0.89% Ro, and HAD 7110 1.45% Ro. (c) Logarithm of number of pores per bin versus pore area for intraorganic pores in HAD 7110, extrapolated from measured pores >25 nm radius, to a radius of 3 nm. (d) Comparison of cumulative porosity obtained from mercury injection (>3 nm radius; black) and image analysis with inorganic (>50 nm radius) and intraorganic (>3 nm radius) porosities superimposed. The red line denotes the minimum value of the extrapolated image porosity, while the green line shows the maximum value. WIC = Wickensen; HAR = Harderode; HAD = Haddessen.

order of 1 nD. This is substantially lower than the permeabilities required to supply gas to a natural or induced fracture network on production timescales, except on subcentimeter length scales. Additional permeability to gas could be provided by porosity, including macroporosity, which is not intraorganic, but is associated with carbonate domains. This includes coccolith-rich fecal pellets and other microfossils which act as microtraps for migrating bitumen and which have dissolved and re-precipitated to form rigid domains. In this study most of the >50 nm pore radius porosity is associated with these domains, and it was formed through the continued generation and expulsion of gas-rich petroleum in a fixed volume. Given the relationship between porosity generation and gas generation, it seems likely that these inorganic pores are gas-filled. There is therefore an inbuilt spatial relationship between carbonate and organic domains which may enhance gas-phase permeability.

In contrast, the clay matrix consists of 1–20 nm diameter pores. If water-filled, these pores will have capillary entry pressures with respect to methane of between 7 (20 nm diameter pore) and 140 MPa (1 nm diameter pore). Displacing water from clay-associated pores will thus be very difficult, so we suggest that gas will only move through these pores if they have been dehydrated over geological time due to dissolution of water into generated gas. For oil especially, the wetting state of each part of the pore system is also a key factor for two phase flow but is poorly constrained in mudstones; we might reasonably assume that OM is oil-wet, but the wetting state of the clay matrix is unknown (e.g., Aplin & Larter, 2005; Kibria et al., 2018; Su et al., 2018).

The results presented in this paper suggest that fluid storage and flow in mudstones, particularly two-phase fluid flow, is strongly influenced by the relative abundance and spatial distribution of clay-rich, OM-rich and carbonate-rich domains. Quantifying the relative amounts of these domains in time and space, albeit on a larger-scale than examined in this paper, might be possible within a predictive palaeoceanographical, sedimentological or sequence stratigraphic framework (e.g., Aplin & Macquaker, 2011; Macquaker &

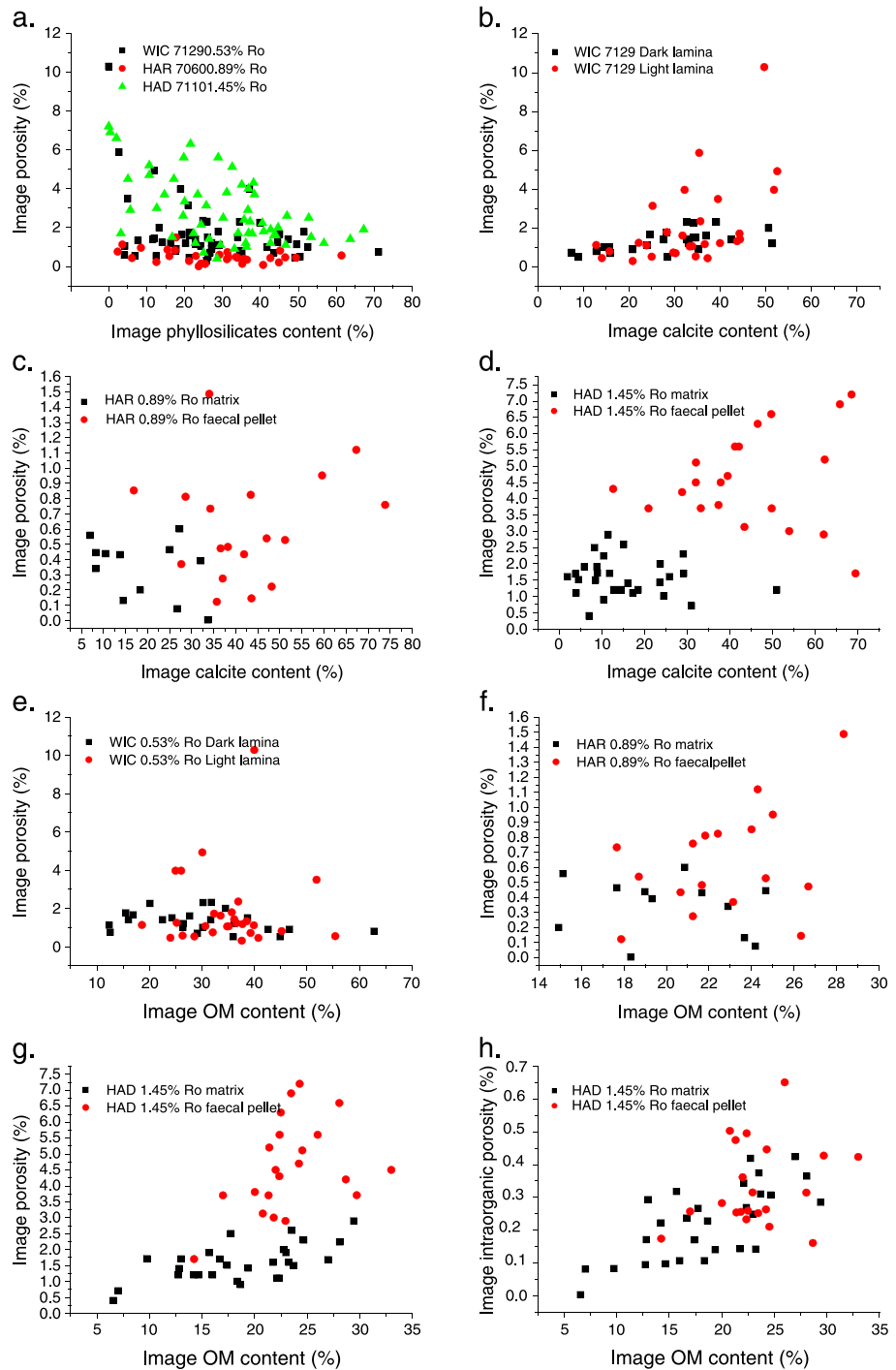


Figure 15. Relationship of image porosity with energy dispersive X-ray-derived (a) phyllosilicate (clay) content, (b–d) calcite content, and (e–h) point-counted organic matter (OM) content in WIC7129, HAR7060, and HAD7110. Each data point represents one BIB-SEM image captured at magnification 10,000X corresponding to a pixel size 6 nm and the minimum resolved pore radius 25 nm. WIC = Wickensen; HAR = Harderode; HAD = Haddessen; BIB-SEM = broad ion beam scanning electron microscopy.

Gawthorpe, 1993; Milliken, 2014; Passey et al., 2010). Palaeogeographic and palaeoceanographical reconstructions are used quite routinely to consider controls on the distribution of mineral, biogenic and organic sedimentary components in both space and time; integrated with the kind of data reported in this paper, we speculate that it may in future be possible to convert mineral or texture maps into flow maps.

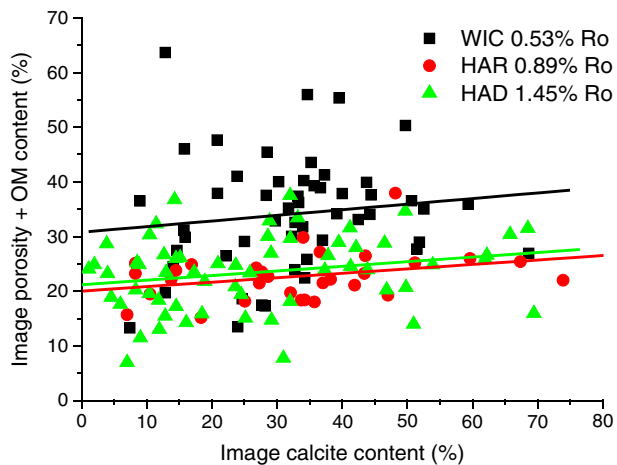


Figure 16. Combined image porosity and organic matter (OM) content and its relationship to energy dispersive X-ray-derived calcite content (vol %). WIC = Wickensen (0.53% Ro), HAR = Harderode (0.89% Ro), and HAD = Haddessen (1.45% Ro). Each data point represents one BIB-SEM image captured at magnification 10,000X, corresponding to a pixel size 6 nm and a minimum resolved pore radius 25 nm. Note that the sum of image porosity and organic matter is similar in peak oil (HAR) and gas window (HAD) samples. BIB-SEM = broad ion beam scanning electron microscopy.

5. Conclusions

We have shown that individually, BIB-SEM, MICP, and CO₂ sorption methods only generate partial descriptions of mudstone pore systems. In combination, they generate a quantitative description of the size distribution and connectivity of pores ranging in size from nanometer to micrometer.

By emplacing quantitative pore size and pore volume data into a detailed mineralogical and textural context, we have shown that the distribution and evolution of pore systems in mudstones can be very usefully considered in terms of the nature of pores within three domains which are common in many mudstones: clay-rich, microfossil-rich, and OM-rich.

Clay-rich domains are microporous and mesoporous at all maturities, with pore radii <10–20 nm. At temperatures below those of gas generation, macropores, which are mainly 25–150 nm radius and comprise 10–15% of total porosity, only occur in microfossils and coccolith-rich fecal pellets. During oil generation, carbonate-related macropores are microtraps for generated bitumen. Porosity is reduced due to bitumen retention and physicochemical compaction. Compaction drives fluid expulsion and retained bitumen becomes a locus for subsequent porosity formation due to gas generation.

Gasification of OM at temperatures above 150 °C increases porosity as the combined result of the reduced volume of solid phase OM and the disso-

lution and reprecipitation of microfossiliferous calcite. Dissolution and reprecipitation yields contact cement which arrests further compactional porosity loss. Most of the generated porosity is not *within* the OM but is physically associated with OM-rich areas within carbonate-related shelter porosity. There is thus a strong genetic link between the evolution of porosity within carbonate-rich and OM-rich domains.

Pore systems are well connected across the full spectrum of pore sizes. However, connectivity is primarily through pores <10 nm radius, and 10–80% (typically 20–40%) of total porosity is associated with pores with radii <~3 nm, within both OM and the clay matrix. Pores with radii >50 nm, that is, those typically observed on SEM images, are only connected through a dense network of much smaller pores, primarily <10 nm radius. The nature of the pore systems implies that permeabilities will be less than ~10–50 nD.

The ability of mudstones to transmit aqueous and hydrocarbon fluids depends not only on the connectivity of pores but also the connectivity of clay-rich and organo-carbonate-rich domains. If clay-rich domains with <1–10 nm pore radii are water filled, very high capillary entry pressures will impede the flow of hydrocarbons associated primarily with organo-carbonate domains.

Understanding and quantifying pore systems in the context of mineralogical or textural domains can be considered as a critical first step in a scaling procedure. Consequently, flow properties may be understood and potentially predicted in terms of the supply and subsequent diagenesis of mud components as functions of palaeoceanographic setting and burial history.

Acknowledgments

This work was supported by the Gas Shales in Europe project funded by Bayerngas, ExxonMobil, GDF Suez, Marathon, Repsol, Schlumberger, Statoil, Total, Vermilion, and Wintershall. We thank Peter Talling, Kitty Milliken, and an anonymous reviewer whose comments helped us clarify several aspects of the paper. The data used are listed in the references and tables.

References

- Abramoff, M., Magalhaes, P., & Ram, S. (2004). Image processing with image. *Journal of Biophotonics International*, 11, 36–42.
- Aplin, A. C., & Larter, S. R. (2005). Fluid flow, pore pressure, wettability, and leakage in mudstone cap rocks, and cap rock seals. In P. Boulton & J. Kaldi (Eds.), *Evaluating fault and cap rock seals, American Association of Petroleum Geologists Hedberg Series* (Vol. 2, pp. 1–12).
- Aplin, A. C., & Macquaker, J. M. S. (2011). Mudstone diversity: Origin and implications for source, seal, and reservoir properties in petroleum systems. *American Association of Petroleum Geologists Bulletin*, 95(12), 2031–2059. <https://doi.org/10.1306/03281110162>
- Behar, F., Lorant, F., & Lewan, M. (2008). Role of NSO compounds during primary cracking of a Type II kerogen and a Type III lignite. *Organic Geochemistry*, 39(1), 1–22. <https://doi.org/10.1016/j.orggeochem.2007.10.007>
- Bernal, J. L. P., & Bello, M. A. (2001). Fractal geometry and mercury porosimetry. Comparison and application of proposed models on building stones. *Applied Surface Science*, 185(1–2), 99–107. [https://doi.org/10.1016/S0169-4332\(01\)00649-3](https://doi.org/10.1016/S0169-4332(01)00649-3)
- Bernard, S., Horsfield, B., Schultz, H.-M., Wirth, R., Schreiber, A., & Sherwood, N. (2011). Geochemical evolution of organic-rich shales with increasing maturity: A STXM and TEM study of the Posidonia shale (lower Toarcian, northern Germany). *Marine and Petroleum Geology*, 31, 70–89.
- Bernard, S., Wirth, R., Schreiber, A., Brown, L., Aplin, A. C., Mathia, E. J., et al. (2013). FIB-SEM and TEM investigations of an organic-rich shale maturation series from the Lower Toarcian Posidonia shale, Germany: Nanoscale pore system and fluid-rock interactions. In W. Camp,

- E. Diaz, & B. Wawak (Eds.), *Electron microscopy of shale hydrocarbon reservoirs*, American Association of Petroleum Geologists Memoir (Vol. 102, pp. 53–66).
- Bernard, S., Wirth, R., Schreiber, A., Schulz, H.-M., & Horsfield, B. (2012). Formation of nanoporous pyrobitumen residues during maturation of the Barnett shale (Fort Worth Basin). *International Journal of Coal Geology*, 103, 3–11. <https://doi.org/10.1016/j.coal.2012.04.010>
- Borst, R. L. (1982). Some effects of compaction and geological time on the pore parameters of argillaceous rocks. *Sedimentology*, 29(2), 291–298. <https://doi.org/10.1111/j.1365-3091.1982.tb01726.x>
- Bour, I., Mattioli, E., & Pittet, B. (2007). Nanofacies analysis as a tool to reconstruct paleoenvironmental changes during the early Toarcian anoxic event. *Palaeogeography, Palaeoclimatology, Palaeoecology*, 249(1-2), 58–79. <https://doi.org/10.1016/j.palaeo.2007.01.013>
- Burnham, A. K., & Braun, R. L. (1990). Development of a detailed model of petroleum formation, destruction, and expulsion from lacustrine and marine source rocks. *Organic Geochemistry*, 16(1-3), 27–39. [https://doi.org/10.1016/0146-6380\(90\)90023-5](https://doi.org/10.1016/0146-6380(90)90023-5)
- Chalmers, G. R. L., & Bustin, R. M. (2012). Geological evaluation of Halfway-Doige-Montney hybrid gas shale-tight gas reservoir, northeastern British Columbia. *Marine and Petroleum Geology*, 38(1), 53–72. <https://doi.org/10.1016/j.marpetgeo.2012.08.004>
- Chalmers, G. R. L., Ross, D. J. K., & Bustin, R. M. (2012). Geological controls on matrix permeability of Devonian gas shales in the Horn River and Liard basins, northeastern British Columbia, Canada. *International Journal of Coal Geology*, 103, 120–131. <https://doi.org/10.1016/j.coal.2012.05.006>
- Clarkson, C. R., Haghshenas, B., Ghanizadeh, A., Qanbari, F., Williams-Kovacs, J. D., Riazi, N., et al. (2016). Nanopores to megafractures: Current challenges and methods for shale gas reservoir and hydraulic fracture characterization. *Journal of Natural Gas Science and Engineering*, 31, 612–657. <https://doi.org/10.1016/j.jngse.2016.01.041>
- Clarkson, C. R., Solano, N., Bustin, R. M., Bustin, A. M. M., Chalmers, G. R. L., He, L., et al. (2013). Pore structure characterization of North American shale gas reservoirs using USANS/SANS, gas adsorption, and mercury intrusion. *Fuel*, 103, 606–616. <https://doi.org/10.1016/j.fuel.2012.06.119>
- Comisky, J.T., Santiago, M., Mccollom, B., Buddhala, A., & Newsham, K.E. (2011). Sample size effects on the application of mercury injection capillary pressure for determining the storage capacity of tight gas and oil shales. Society of Petroleum Engineers, Canadian Unconventional Resources Conference, 15–17 November 2011, Calgary, Alberta, Canada.
- Compressed Gas Association (1990). *Handbook of compressed gases*, (3rd ed.). New York: Van Nostrand Reinhold.
- Conner, W. C., Cevallos-Candau, J. F., Weist, E. L., Pajares, J., Mendiroz, S., & Cortés, A. (1986). Characterisation of pore structure: Porosimetry and sorption. *Langmuir*, 2, 151–154.
- Coskey, R.J. (2001). Bakken and Niobrara plays. A geologic comparison. Tight Oil from Shale Plays World Congress, 31 January – 1 February 2011 (Online).
- Curtis, M. E., Sondergeld, C. H., Ambrose, R. J., & Rai, C. S. (2012). Microstructural investigation of gas shales in two and three dimensions using nanometer-scale resolution imaging. *American Association of Petroleum Geologists Bulletin*, 96(4), 665–677. <https://doi.org/10.1306/08151110188>
- Day-Stirrat, R. J., Aplin, A. C., Śródoń, J., & Van Der Pluijm, B. A. (2008). Diagenetic reorientation of phyllosilicate minerals in Paleogene mudstones of the Podhale Basin, southern Poland. *Clays and Clay Minerals*, 56, 98–109.
- Day-Stirrat, R. J., Flemings, P. B., Yao, Y., Aplin, A. C., & Van Der Pluijm, B. A. (2012). The fabric of consolidation in Gulf of Mexico mudstones. *Marine Geology*, 295-298, 77–85. <https://doi.org/10.1016/j.margeo.2011.12.003>
- Desbois, G., Urai, J. L., & Kukla, P. A. (2009). Morphology of the pore space in claystones—Evidence from BIB/FIB ion beam sectioning and cryo-SEM observations. *eEarth*, 4(1), 15–22. <https://doi.org/10.5194/ee-4-15-2009>
- Dewit, L. A., & Scholten, J. J. F. (1975). Studies on pore structure of adsorbents and catalysts: II. Pore size distribution in synthetic chrysotile: The classical and corrected Kelvin equation applied to nitrogen capillary condensation. *Journal of Catalysis*, 36(1), 30–35. [https://doi.org/10.1016/0021-9517\(75\)90006-8](https://doi.org/10.1016/0021-9517(75)90006-8)
- Diamond, S. (1970). Pore size distributions in clays. *Clays and Clay Minerals*, 18(1), 7–23. <https://doi.org/10.1346/CCMN.1970.0180103>
- Fishman, N. S., Hackley, P. C., Lowers, H. A., Hill, R. J., Egenhoff, S. O., Eberl, D. D., & Blum, A. E. (2012). The nature of porosity in organic-rich mudstones of the Upper Jurassic Kimmeridge clay formation, North Sea, offshore United Kingdom. *International Journal of Coal Geology*, 103, 32–50. <https://doi.org/10.1016/j.coal.2012.07.012>
- Friesen, W. I., & Mikula, R. J. (1988). Mercury porosimetry of coals: Pore volume distribution and compressibility. *Fuel*, 67(11), 1516–1520. [https://doi.org/10.1016/0016-2361\(88\)90069-5](https://doi.org/10.1016/0016-2361(88)90069-5)
- Hall, P. L., Mildner, D. F. R., & Borst, R. L. (1983). Pore size distribution of shaly rock by small angle neutron scattering. *Applied Physics Letters*, 43(3), 252–254. <https://doi.org/10.1063/1.94316>
- Hall, P. L., Mildner, D. F. R., & Borst, R. L. (1986). Small-angle scattering studies of the pore spaces of shaly rocks. *Journal of Geophysical Research*, 91(B2), 2183–2192. <https://doi.org/10.1029/JB091iB02p02183>
- Hill, P. R. (1987). Chalk solution structures in cores from Deep Sea Drilling Project Leg 94, Norfolk Virginia to St. Johns Newfoundland. In W. F. Ruddiman & R. B. Kidd (Eds.), *Initial reports of the Deep Sea Drilling Project Leg 94* (pp. 1129–1143). Washington, DC: U.S. Printing Office.
- Houben, M. E., Desbois, G., & Urai, J. L. (2013). Pore morphology and distribution in the Shaly facies of Opalinus clay (Mont Terri, Switzerland): Insights from representative 2D BIB-SEM investigations on mm to nm scale. *Applied Clay Science*, 71, 82–97. <https://doi.org/10.1016/j.clay.2012.11.006>
- Houben, M. E., Desbois, G., & Urai, J. L. (2014). A comparative study of representative 2D microstructures in Shaly and Sandy facies of Opalinus clay (Mont Terri, Switzerland) inferred from BIB-SEM and MIP methods. *Marine and Petroleum Geology*, 49, 143–161. <https://doi.org/10.1016/j.marpetgeo.2013.10.009>
- Hower, J., Eslinger, E. V., Hower, M. E., & Perry, E. A. (1976). Mechanism of burial metamorphism of argillaceous sediment: 1. Mineralogical and chemical evidence. *Geological Society of America Bulletin*, 87(5), 725–737. [https://doi.org/10.1130/0016-7606\(1976\)87<725:MOBMOA>2.0.CO;2](https://doi.org/10.1130/0016-7606(1976)87<725:MOBMOA>2.0.CO;2)
- Isaacs, C. M. (1981). Porosity reduction during diagenesis of the Monterey formation, Santa Barbara coastal area, California. In R. E. Garrison & R. G. Douglas (Eds.), *The Monterey Formation and related siliceous rocks of California* (pp. 257–271). Los Angeles: SEPM Society for Sedimentary Geology Pacific Section.
- Jarvie, D. M., Hill, R. J., Ruble, T. E., & Pollastro, R. M. (2007). Unconventional shale-gas systems: The Mississippian Barnett shale of north-central Texas as one model for thermogenic shale gas assessment. *American Association of Petroleum Geologists Bulletin*, 91(4), 475–499. <https://doi.org/10.1306/12190606068>
- Joyner, L. G., Barrett, E. P., & Skold, R. (1951). The determination of pore volume and area distributions in porous substances. II. Comparison between nitrogen isotherm and mercury porosimeter methods. *Journal of the American Chemical Society*, 73(7), 3155–3158. <https://doi.org/10.1021/ja01151a046>

- Justwan, H., & Dahl, B. (2005). Quantitative hydrocarbon potential mapping and organofacies study in the Greater Balder Area, Norwegian North Sea. *Petroleum Geology Conference Series*, 6(1), 1317–1329. <https://doi.org/10.1144/0061317>
- Keller, L. M., Schuetz, P., Erni, R., Rossell, M. D., Lucas, F., Gasser, P., & Holzer, L. (2013). Characterization of multi-scale microstructural features in Opalinus clay. *Microporous and Mesoporous Materials*, 170, 83–94. <https://doi.org/10.1016/j.micromeso.2012.11.029>
- Kibria, M. G., Hua, Q., Liu, H., Zhang, Y., & Kang, J. (2018). Pore structure, wettability, and spontaneous imbibition of Woodford shale, Permian Basin, West Texas. *Marine and Petroleum Geology*, 91, 735–748.
- King, H. E. Jr., Eberle, A. P. R., Walters, C. C., Kliwer, C. E., Ertas, D., & Huynh, C. (2015). Pore architecture and connectivity in gas shale. *Energy & Fuels*, 29, 1375–1390.
- Klaver, J., Desbois, G., Littke, R., & Urai, J. L. (2012). BIB-SEM characterization of pore space morphology and distribution in postmature to overmature samples from the Haynesville and Bossier Shales. *Marine and Petroleum Geology*, 59, 451–466.
- Klaver, J., Desbois, G., Littke, R., & Urai, J. L. (2015). BIB-SEM characterization of pore space morphology and distribution in postmature to overmature samples from the Haynesville and Bossier Shales. *Marine and Petroleum Geology*, 59, 451–466. <https://dx.doi.org/10.1016/j.marpetgeo.2014.09.020>
- Klaver, J., Desbois, G., Urai, J. L., & Littke, R. (2012). BIB-SEM study of the pore space morphology in early mature Posidonia shale from the Hils area, Germany. *International Journal of Coal Geology*, 103, 12–25. <https://doi.org/10.1016/j.coal.2012.06.012>
- Kliwer, C. E., Walters, C. C., Huynh, C., Scipioni, L., Elswick, D., Jonk, R., et al. (2012). Geological applications of helium ion microscopy. Analysis and visualization of the pore networks within shale and coal. *Imaging and Microscopy*, 2012, 15–18.
- Ko, L. T., Loucks, R. G., Ruppel, S. C., Zhang, T., & Peng, S. (2017). Origin and characterization of Eagle Ford pore networks in the south Texas Upper Cretaceous shelf. *American Association of Petroleum Geologists Bulletin*, 101(03), 387–418. <https://doi.org/10.1306/08051616035>
- Kuo, L.-C., Hardy, H. H., & Owilli-Eger, A. S. C. (1995). Quantitative modeling of organic matter connectivity in source rocks using fractal geostatistical analysis. *Organic Geochemistry*, 23(1), 29–42. [https://doi.org/10.1016/0146-6380\(94\)00111-D](https://doi.org/10.1016/0146-6380(94)00111-D)
- Lewan, M. D. (1997). Experiments on the role of water in petroleum formation. *Geochimica et Cosmochimica Acta*, 61(17), 3691–3723. [https://doi.org/10.1016/S0016-7037\(97\)00176-2](https://doi.org/10.1016/S0016-7037(97)00176-2)
- Leythaeuser, D., Littke, R., Radke, M., & Schaefer, R. G. (1988). Geochemical effects of petroleum migration and expulsion from Toarcian source rocks in the Hils syncline area, NW-Germany. *Organic Geochemistry*, 13(1-3), 489–502. [https://doi.org/10.1016/0146-6380\(88\)90070-8](https://doi.org/10.1016/0146-6380(88)90070-8)
- Littke, R., Baker, D. R., Leythaeuser, D., & Rullkötter, J. (1991). Keys to the depositional history of the Posidonia shale (Toarcian) in the Hils syncline, northern Germany. In R. V. Tyson & T. H. Pearson (Eds.), *Modern and ancient continental shelf anoxia, Geological Society Special Publication* (Vol. 58, pp. 311–333). London, UK: The Geological Society of London.
- Loucks, R. G., Reed, R. M., Ruppel, S. C., & Hammes, U. (2012). Spectrum of pore types and networks in mudrocks and a descriptive classification for matrix-related mudrock pores. *American Association of Petroleum Geologists Bulletin*, 96(6), 1071–1098. <https://doi.org/10.1306/08171111061>
- Loucks, R. G., Reed, R. M., Ruppel, S. C., & Jarvie, D. M. (2009). Morphology, genesis and distribution of nanometer-scale pores in siliceous mudstones of the Mississippian Barnett shale. *Journal of Sedimentary Research*, 79(12), 848–861. <https://doi.org/10.2110/jsr.2009.092>
- Macquaker, J. H. S., & Gawthorpe, R. L. (1993). Mudstone lithofacies in the Kimmeridge clay formation, Wessex Basin, southern England: Implications for the origin and controls of the distribution of mudstones. *Journal of Sedimentary Petrology*, 63, 1129–1143.
- Mastalerz, M., Schimmelmann, A., Drobnik, A., & Chen, Y. (2013). Porosity of Devonian and Mississippian New Albany shale across a maturation gradient: Insights from organic petrology, gas adsorption, and mercury intrusion. *Association of Petroleum Geologists Bulletin*, 97(10), 1621–1643. <https://doi.org/10.1306/04011312194>
- Mathia, E. J. (2015). Geological Evaluation of Posidonia and Wealden organic-rich shales: Geochemical and diagenetic controls on pore system evolution. (Doctoral thesis, Newcastle University, Newcastle upon Tyne, United Kingdom). Retrieved from <https://theses.ncl.ac.uk/dspace/handle/10443/2783>
- Mathia, E. J., Bowen, L., Thomas, K. M., & Aplin, A. C. (2016). Evolution of porosity and pore types in organic-rich, calcareous, lower Toarcian Posidonia shale. *Marine and Petroleum Geology*, 75, 117–139. <https://doi.org/10.1016/j.marpetgeo.2016.04.009>
- Michels, R., Langlois, E., Ruau, O., Mansuy, L., Elie, M., & Landais, P. (1996). Evolution of asphaltenes during artificial maturation: A record of the chemical processes. *Energy & Fuels*, 10(1), 39–48. <https://doi.org/10.1021/ef9501410>
- Mildner, D. F. R., Rezvani, R., Hall, P. L., & Borst, R. L. (1986). Small-angle scattering of shaly rocks with fractal interfaces. *Applied Physics Letters*, 48(19), 1314–1316. <https://doi.org/10.1063/1.96964>
- Milliken, K. L. (2014). A compositional classification for grain assemblages in fine-grained sediments and sedimentary rocks. *Journal of Sedimentary Research*, 84(12), 1185–1199. <https://doi.org/10.2110/jsr.2014.92>
- Milliken, K. L., & Curtis, M. E. (2016). Imaging pores in sedimentary rocks: Foundations of porosity prediction. *Marine and Petroleum Geology*, 73, 590–608. <https://doi.org/10.1016/j.marpetgeo.2016.03.020>
- Milliken, K. L., Esch, W. L., Reed, R. M., & Zhang, T. (2012). Grain assemblages and strong diagenetic overprinting in siliceous mudrocks, Barnett shale (Mississippian), Fort Worth Basin, Texas. *American Association of Petroleum Geologists Bulletin*, 96(8), 1553–1578. <https://doi.org/10.1306/12011111129>
- Milliken, K. L., & Olson, T. (2017). Silica diagenesis, porosity evolution, and mechanical behaviour in siliceous mudstones, Mowry shale (cretaceous), Rocky Mountains, U.S.a. *Journal of Sedimentary Research*, 87(4), 366–387. <https://doi.org/10.2110/jsr.2017.24>
- Milliken, K. L., Rudnicki, M., Awwiler, D. N., & Zhang, T. (2013). Organic matter-hosted pore system, Marcellus formation (Devonian), Pennsylvania. *American Association of Petroleum Geologists Bulletin*, 97(2), 177–200. <https://doi.org/10.1306/07231212048>
- Modica, C. J., & Lapierre, S. G. (2012). Estimation of kerogen porosity in source rocks as a function of thermal transformation: Example from the Mowry shale in the Powder River Basin of Wyoming. *American Association of Petroleum Geologists Bulletin*, 96(1), 87–108. <https://doi.org/10.1306/04111110201>
- Nordgård Bolås, H. M., Hermanrud, C., & Teige, G. M. G. (2004). Origin of overpressures in shales: Constraints from basin modeling. *American Association of Petroleum Geologists Bulletin*, 88(2), 193–211. <https://doi.org/10.1306/10060302042>
- Padhy, G. S., Lemaire, C., Amirharaj, E. S., & Ioannidis, M. A. (2007). Pore size distribution in multiscale porous media as revealed by DDIF-NMR, mercury porosimetry and statistical image analysis. *Colloids and Surfaces A: Physicochemical and Engineering Aspects*, 300(1-2), 222–234. <https://doi.org/10.1016/j.colsurfa.2006.12.039>
- Passey, Q.R., Bohacs, K.M., Esch, W. L., Klimentidis, R., & Sinha, S. (2010). From oil-prone source rock to gas-producing shale reservoir—Geologic and petrophysical characterization of unconventional shale-gas reservoirs. *Proceedings of the North American Unconventional Gas Conference and Exhibition. Society of Petroleum Engineers*, Paper 131350, 29p.
- Pommer, M., & Milliken, K. (2015). Pore types and pore-size distributions across thermal maturity, Eagle Ford formation, southern Texas. *American Association of Petroleum Geologists Bulletin*, 99(09), 1713–1744. <https://doi.org/10.1306/03051514151>

- Rexer, T. F. T., Mathia, E. J., Aplin, A. C., & Thomas, K. M. (2014). High-pressure methane adsorption and characterization of pores in Posidonia shales and isolated kerogens. *Energy & Fuels*, 28(5), 2886–2901. <https://doi.org/10.1021/ef402466m>
- Roduit, N. (2008). JMicroVision: Image analysis toolbox for measuring and quantifying components of high-definition images. *Version 1.2.7*. Software available for free download at <http://www.jmicrovision.com/> Accessed August, 2011.
- Röhl, H. J., & Schmid-Röhl, A. (2005). Lower Toarcian (upper Liassic) black shales of the central European epicontinental basin: A sequence stratigraphic case study from the SW German Posidonia shale. In B. L. Harris (Ed.), *The deposition of organic carbon-rich sediments: Models, mechanisms, and consequences*, Society for Sedimentary Geology Special Publication (Vol. 82, pp. 165–189). <https://doi.org/10.2110/pec.05.82.0165>
- Röhl, H. J., Schmid-Röhl, A., Oschmann, W., Frimmel, A., & Schwark, L. (2001). The Posidonia shale (lower Toarcian) of SW-Germany: An oxygen-depleted ecosystem controlled by sea level and palaeoclimate. *Palaeogeography, Palaeoclimatology, Palaeoecology*, 165(1-2), 27–52. [https://doi.org/10.1016/S0031-0182\(00\)00152-8](https://doi.org/10.1016/S0031-0182(00)00152-8)
- Ross, D. J. K., & Bustin, R. M. (2009). The importance of shale composition and pore structure upon gas storage potential of shale gas reservoirs. *Marine and Petroleum Geology*, 26(6), 916–927. <https://doi.org/10.1016/j.marpetgeo.2008.06.004>
- Rullkötter, J., Leythaeuser, D., Horsfield, B., Littke, R., Mann, U., Müller, P. J., et al. (1988). Organic matter maturation under the influence of a deep intrusive heat source: A natural experiment for quantitation of hydrocarbon generation and expulsion from a petroleum source rock (Toarcian shale, northern Germany). *Organic Geochemistry*, 13(4-6), 847–856. [https://doi.org/10.1016/0146-6380\(88\)90237-9](https://doi.org/10.1016/0146-6380(88)90237-9)
- Schlömer, S., & Krooss, B. M. (1997). Experimental characterization of the hydrocarbon sealing efficiency of cap rocks. *Marine and Petroleum Geology*, 14, 563–578.
- Schowalter, T. T. (1979). Mechanics of secondary hydrocarbon migration and entrapment. *American Association of Petroleum Geologists Bulletin*, 63, 723–760.
- Sing, K. S. W., Everett, D. H., Haul, R. A. W., Moscou, L., Pierotti, R. A., Rouquerol, J., & Siemieniowska, T. (1985). Reporting physisorption data for gas solid systems with special reference to the determination of surface-area and porosity (recommendations 1984). *Pure and Applied Chemistry*, 57(4), 603–619. <https://doi.org/10.1351/pac198557040603>
- Smith, J. E. (1971). The dynamics of shale compaction and evolution of pore fluid pressure. *Mathematical Geology*, 3(3), 239–263. <https://doi.org/10.1007/BF02045794>
- Song, Y., Davy, C. A., Bertier, P., & Troadec, D. (2016). Understanding fluid transport through claystones from their 3D nanoscopic pore network. *Microporous and Mesoporous Materials*, 228, 64–85. <https://doi.org/10.1016/j.micromeso.2016.03.023>
- Stock, A. T., Littke, R., Schwarzbauer, J., Horsfield, B., & Hartkopf-Fröder, C. (2017). Organic geochemistry and petrology of Posidonia shale (lower Toarcian, western Europe)—The evolution from immature oil-prone to overmature dry gas-producing kerogen. *International Journal of Coal Geology*, 176–177, 36–48. <https://doi.org/10.1016/j.coal.2017.04.016>
- Su, S., Jiang, Z., Shan, X., Zhu, Y., Wang, P., Luo, X., et al. (2018). The wettability of shale by NMR measurements and its controlling factors. *Journal of Petroleum Science and Engineering*, 169, 309–316. <https://doi.org/10.1016/j.petrol.2018.05.067>
- Suuberg, E., Deevi, S. C., & Yun, Y. (1995). Elastic behaviour of coals studied by mercury porosimetry. *Fuel*, 74(10), 1522–1530. [https://doi.org/10.1016/0016-2361\(95\)00110-Q](https://doi.org/10.1016/0016-2361(95)00110-Q)
- Tao, S., Wang, Y., Tang, D., Wu, D., Xu, H., & He, W. (2012). Organic petrology of Fukang Permian Lucaogou formation oil shales at the northern foot of Bogda Mountain, Junggar Basin, China. *International Journal of Coal Geology*, 99, 27–34. <https://doi.org/10.1016/j.coal.2012.05.001>
- Toda, Y., & Toyoda, S. (1972). Application of mercury porosimetry to coal. *Fuel*, 51(3), 199–201. [https://doi.org/10.1016/0016-2361\(72\)90080-4](https://doi.org/10.1016/0016-2361(72)90080-4)
- Vandenbroucke, M., Behar, F., San Torcuato, A., & Rullkötter, J. (1993). Kerogen maturation in a reference kerogen Type II series: The Toarcian shales of the Hils syncline, NW Germany. *Organic Geochemistry*, 20(7), 961–972. [https://doi.org/10.1016/0146-6380\(93\)90106-L](https://doi.org/10.1016/0146-6380(93)90106-L)
- Vandenbygaart, A. J., & Protz, R. (1999). The representative elementary area REA in studies of quantitative soil micromorphology. *Geoderma*, 89(3-4), 333–346. [https://doi.org/10.1016/S0016-7061\(98\)00089-5](https://doi.org/10.1016/S0016-7061(98)00089-5)
- Wang, P., Jiang, Z., Chen, L., Yin, L., Li, Z., Zhang, C., et al. (2016). Pore structure characterization for the Longmaxi and Niutitang shales in the upper Yangtze platform, South China: Evidence from focused ion beam-He ion microscopy, nano-computerized tomography and gas adsorption analysis. *Marine and Petroleum Geology*, 77, 1323–1337. <https://doi.org/10.1016/j.marpetgeo.2016.09.001>
- Washburn, E. W. (1921). The dynamics of capillary flow. *Physical Review*, 17(3), 273–283. <https://doi.org/10.1103/PhysRev.17.273>
- Webb, P. A. (2001). *An introduction to the physical characterization of materials by mercury intrusion porosimetry with emphasis on reduction and presentation of experimental data* (p. 23). Norcross, Georgia: Micromeritics Instrument Corporation.
- Wilhelms, A., Larter, S. R., Leythaeuser, D., & Dypvik, H. (1990). Recognition and quantification of the effects of primary migration in a Jurassic clastic source-rock from the Norwegian. *Organic Geochemistry*, 16(1-3), 103–113. [https://doi.org/10.1016/0146-6380\(90\)90030-4](https://doi.org/10.1016/0146-6380(90)90030-4)
- Yang, Y., & Aplin, A. C. (1998). Influence of lithology and compaction on the pore size distribution and modelled permeability of some mudstones from the Norwegian margin. *Marine and Petroleum Geology*, 15(2), 163–175. [https://doi.org/10.1016/S0264-8172\(98\)00008-7](https://doi.org/10.1016/S0264-8172(98)00008-7)
- Yang, Y., & Aplin, A. C. (2007). Permeability and petrophysical properties of 30 natural mudstones. *Journal of Geophysical Research*, 112, B03206. <https://doi.org/10.1029/2005JB004243>
- Zwietering, P., & Koks, H. L. T. (1954). Pore size distribution of porous iron. *Nature*, 173(4406), 683–684. <https://doi.org/10.1038/173683a0>